Journal of Scientific Computing (2020) 83:31
https://doi.org/10.1007/s10915-020-01214-z

Eulerian Model for Simulating Multi-Fluid Flows with an Arbitrary Number of Immiscible Compressible Components

Chao Zhang[1] · **Igor Menshov**[2,3]

Received: 7 November 2019 / Revised: 17 March 2020 / Accepted: 8 April 2020

Abstract
A $(2N+1)$-equation model to simulate the flow of N ($N \geq 3$) immiscible compressible fluids separated with interfaces is proposed. The model is based on the single velocity diffuse-interface method and includes $N-1$ advection equations for fluid volume fractions. Solving the advection equations with a non-linear high-order scheme commonly results in the violation of the non-negativity constraint that any arbitrary partial sum of volume fractions should be in the interval [0, 1]. First, it is shown that this constraint can be met if the $N-1$ advection equations are solved for some rational functions of volume fractions rather than for volume fractions themselves. The non-linear sub-cell slope reconstruction (MUSCL-type and THINC) with the proposed rational advection functions is proved to be non-oscillatory and provide the distribution of volume fractions satisfying the non-negativity constraint. Second, it is proved that the PV property (preservation of constant-pressure and constant-velocity equilibrium) is maintained providing that linear functions of volume fractions are used in the advection equations. We suggest two ways for resolving the contradiction in choosing the advection functions (functions of volume fractions) in accordance with the non-negativity constraint and the PV property. We also adopt two numerical methods—the Roe-type scheme and the HLLC scheme to solve the governing equations. Finally, the proposed numerical model is tested with several benchmark problems. The results obtained demonstrate robustness and effectiveness of the proposed numerical approach in solving multi-fluid flows with large interface deformations.

Keywords Multi-fluid dynamics · Diffuse-interface methods · High-order scheme · Eulerian grid

Mathematics Subject Classification 76T30 · 35L65

Electronic supplementary material The online version of this article (https://doi.org/10.1007/s10915-020-01214-z) contains supplementary material, which is available to authorized users.

✉ Chao Zhang
zhang-c@mail.ru

Extended author information available on the last page of the article

Published online: 24 April 2020

1 Introduction

Modeling compressible multi-material flows with sharp material interfaces is of great interest in a wide range of industrial and technical applications, such as the underwater explosion problem [34,49,52], gas release from a subsea natural gas pipeline [7,14,16], mixing processes [10], bubbly flows [44,45] and so on. In these problems, accurate resolution of the material interface motion poses quite challenging theoretical and computational tasks. So far, several models and numerical methods have been proposed to tackle the problem of interface calculation.

The material interface is typically represented by volume fractions, thermodynamic parameters or level-set functions. According to the treatment of material interfaces numerical methods can be categorized into two groups: interface-capturing methods and interface-tracking methods. The latter include volume-of-fluid [25], and moment-of-fluid [12,13], Arbitrary Lagrangian Eulerian (ALE) [6,18,33,35], free Lagrange [4], front tracking [8,19,20,58], level set/ghost fluid [38,42,43] schemes, and the ghost fluid method [15]. Interface-tracking methods are capable of locating interface between materials with different equations of state without introducing spurious oscillations. However, most interface-tracking methods suffer from two defects. The first is that the evolution of the interface with time can lead to serious distortions of the computational grid and deteriorations of the accuracy; second, they may not be conservative in the vicinity of the interface, and prone to generate errors in locating the material interface. Solutions to these problems exist, for example the cut-cell method on a fixed mesh [39] and the conservative level set method [40,41].

On the contrary, interface-capturing methods [1,2,9,28,29,36,47,51–54,57,59,60] are conservative by allowing the material-related parameters to diffuse near the material interface. These parameters can be thermodynamic parameters in the equation of state (EOS) or volume fractions governed by the transport equation. For the interface-capturing method, it is vital to maintain the sharpness of the material interface. Various interface-sharpening methods are proposed, among which are the interface compression method [22,23,39,52], the limited downwind scheme [11,32], the anti-diffusion method based on the flux correction algorithm [57], the WENO scheme [9,28,50], the THINC scheme [56,62], and the method based on the solution of the composite Riemann problem (CRP) [36,64]. The THINC scheme is rather effective and simple in implementation, thus we couple it with the approach developed in the present work. Moreover, a thermodynamically consistent model for the mixture of materials should be applied in the diffusion zone near the interface. We apply the equation of state for the mixture based on the isobaric closure assumption.

One of the most studied interface-capturing models is a five-equation model of Allaire et al. [2] for two-fluid flows. Although Allaire et al. [2] made a thorough analysis on mathematical properties of this model for the case of two components, there remains a notable gap in research on the situation of $N(N \geq 3)$ components. As noted in [2], one can obtain a generalized model to treat more than two fluids by adding a partial density conservation equation and a volume fraction advection equation for each fluid. For this generalized model, from the assumption of a saturated mixture follows that the volume fractions are non-negative and sum to one (termed as the "non-negativity constraint" in the following). Once this condition is violated, spurious oscillations and non-physical solutions arise. When the generalized model is extended to high order schemes, such as MUSCL, WENO or coupled with the interface-sharpening technique, such as THINC, the above mentioned conditions may be violated. The root of the problem is non-linearity of the reconstruction process.

Jaouen et al. [27] proposed a numerical method for the transport of an arbitrary number of components by modifying the numerical flux of the limited downwind scheme [11]. This method ensures the non-negativity constraint for volume fractions when the Lax–Wendroff scheme or the limited downwind scheme is used. However, it fails when coupled with the MUSCL scheme or other interface-sharpening techniques based on sub-cell reconstruction.

Friess and Kokh [17] proposed a $(2N+2)$-equation model for compressible flows, which is the extension of the five-equation model to the case of $N(N \geq 3)$ materials. This model consists of $(2N+2)$ equations including N conservation equations for partial densities, the conservation equation for momentum, the conservation equation for energy, and N advection equations for volume fractions. The limited downwind scheme for an arbitrary number of components proposed by Jaouen et al. [27] is utilized to reduce numerical diffusion.

In the present work, we propose a simple and robust method to solve the advection equations for an arbitrary number of components. Instead of the advection equations for volume fractions that are used in the work of Allaire et al. [2], Jaouen et al. [27], and Friess et al. [17], we introduce new advection equations for specially defined functions (termed as "advection functions" in the following). Theses functions are chosen so that direct solution of the advection equations with non-linear slope reconstruction (in the following we use "reconstruction" for simplicity) schemes would naturally maintain constraints on volume fractions.

On the basis of this method, we further propose a $(2N+1)$-equation model for multi-fluid compressible flows of $N(N \geq 3)$ components. For this model, we propose a technique to maintain non-negative volume fraction constraints and prevent any spurious oscillations in the vicinity of the material interfaces. We use properly chosen different advection functions in updating and reconstructing volume fractions, namely:

(1) Updating is fulfilled with linear functions of volume fractions; this ensures the PV property and maintains the constant-pressure equilibrium.
(2) Reconstructing volume fractions is performed with the rational advection functions properly chosen so that the aforementioned constraint conditions for volume fractions can be satisfied.

After implementing the above algorithm, a weak TVD (total variation diminishing) property for cell-averaged volume fractions can be met with a simple correction step.

The model we are developing can be viewed as a multi-fluid extension to the five-equation model [2]. It can also be derived from a non-equilibrium model of Baer–Nunziato type [3,26,30] by means of performing asymptotic analysis in the limit of zero relaxation time. The model possesses the following properties: consistency of the closure model, hyperbolicity, and entropy condition. The consistency property ensures that all primitive variables can be recovered from the conserved variables and vice versa. This property is proved for the generalized Van der Waals EOS and the Mie–Gruneisen EOS. As a generalization of the five-equation model, our model also uses the conservative equations and isobaric closure relations. To sharpen the material interface, we apply the MUSCL and THINC schemes to reconstruct advection functions rather than volume fractions; the latter are then recovered from the reconstructed advection functions.

The paper is organized as follows. In Sect. 2, we introduce and discuss the numerical method to solve the advection equations for an arbitrary number of components. In Sect. 3, we formulate the $(2N+1)$-equation model and proof some relevant mathematical properties. In Sect. 4, we deal with numerical schemes for discretization and solution of the model. In Sect. 5, we examine our model and algorithm with some typical 1D and 2D tests. Finally, a short conclusion is given in Sect. 6.

2 Advection Equations for an Arbitrary Number of Components

In this section, we deal with the numerical transport of an arbitrary number of components in a prescribed velocity field. For each component, we introduce a color function z_j that represents the volume fraction of the j-th component. The transport of N components are governed by the following system of advection equations:

$$\frac{\partial z_j}{\partial t} + \mathbf{u} \cdot \text{grad} z_j = 0, \quad j \in \Phi = \{1, 2, 3, \ldots, N\}. \tag{1}$$

The color functions are constrained by the following equation

$$\sum_{j=1}^{N} z_j = 1. \tag{2}$$

Thus, only $N - 1$ equations of (1) are independent. In the following, we consider the last $N - 1$ equations, i.e.

$$\frac{\partial z_j}{\partial t} + \mathbf{u} \cdot \text{grad} z_j = 0, \quad j \in \Psi = \{2, 3, \ldots, N\}. \tag{3}$$

As mentioned above, we want the volume fractions to meet the following physical constraints:

$$z_j \in [0, 1] \quad j \in \Psi, \tag{4}$$

$$\sum_{j \in \Lambda} z_j \leq 1, \quad j \in \Lambda \subset \Psi, \tag{5}$$

where Λ is an arbitrary subset of Ψ.

The condition (5) indicates that an arbitrary partial sum of the volume fractions should not exceed 1. If the initial conditions are given in such way that the conditions (4) and (5) are satisfied, the volume fractions in the following time steps should also meet these conditions. The first-order approximate Riemann solvers (Roe-type and HLLC) give reasonable solutions that satisfy this requirement, however, they introduce strong numerical dissipation and material interfaces is smearing in the course of time.

To reduce this numerical effect, higher order accurate schemes and interface-sharpening techniques are employed. However, non-linearity of higher-order schemes and interface-sharpening techniques results in violation of the conditions (4) and (5) as can be seen below. To cope with the situation, we propose to solve advection equations for specific functions of volume fractions instead of the volume fractions themselves. These specific functions are defined as

$$f_j = f_j (z_2, z_3, \ldots, z_N), \quad j \in \Psi. \tag{6}$$

The corresponding system of advection equations becomes

$$\frac{\partial f_j}{\partial t} + \mathbf{u} \cdot \text{grad} f_j = 0, \quad j \in \Psi. \tag{7}$$

The functions $f_j (z_2, z_3, \ldots, z_N)$ are termed as advection functions henceforth.

After obtaining the solution of f_j, we recover z_j by using Eq. (6). To recover z_j from f_j, the Jacobian should not be zero, i.e.

$$J = \begin{vmatrix} \partial f_2/\partial z_2 & \partial f_2/\partial z_3 & \cdots & \partial f_2/\partial z_N \\ \partial f_3/\partial z_2 & \partial f_3/\partial z_3 & \cdots & \partial f_3/\partial z_N \\ \vdots & \vdots & \vdots & \vdots \\ \partial f_N/\partial z_2 & \partial f_N/\partial z_3 & \cdots & \partial f_N/\partial z_N \end{vmatrix} \neq 0. \tag{8}$$

We consider the one-dimension advection problem. The FVM (finite volume method) discretization of Eq. (7) with the upwind scheme on a uniform grid gives

$$f_{j,i}^{n+1} = f_{j,i}^{n} - u\lambda \left(f_{j,i+1/2}^{n} - f_{j,i-1/2}^{n} \right), \tag{9}$$

$$f_{j,i+1/2}^{n} = \frac{u + |u|}{2} f_{j,i+1/2}^{L} + \frac{u - |u|}{2} f_{j,i+1/2}^{R}, \tag{10}$$

where u is the advection velocity, the subscript i and the superscript n indicate cell index and time level, respectively, $\lambda = \Delta t/\Delta x$, Δt is the time step, Δx is the spatial step, the superscripts L and R denote the interpolated values on the left and right of the cell faces, respectively.

Choosing advection functions is important for the scheme because it defines whether the higher-order extension to the scheme will succeed or fail. When the initial values of advection functions in the i-th cell $f_{j,i}$ are within [0, 1], the evolved values of $f_{j,i}$ in following time steps are also within [0, 1] because of passive advection. Apart from that, the numerical scheme should also ensure that the restored volume fractions in the i-th cell $z_{j,i} = z_{j,i}(f_{2,i}, f_{3,i}, \ldots, f_{N,i})$ also meet conditions (4) and (5).

The conditions (4) and (5) are satisfied for the case of $N = 2$ components, even if the non-linear reconstruction scheme MUSCL, WENO or the sharpening technique THINC is applied. In fact, in this case conditions (4) and (5) are equivalent. However, this is not the case in the model with $N \geq 3$ components. When the non-linear reconstruction schemes are applied to advection functions, the conditions (4) and (5) may be violated resulting in oscillatory solutions. In order to keep the conditions (4) and (5), we will require the reconstructed values on cell faces to meet also these conditions.

We now demonstrate the origin of the problem when the numerical scheme is coupled with the MINMOD scheme. For the case of $N = 3$, three sets of advection functions are considered:

$$f_2(z_2, z_3) = z_2,\ f_3(z_2, z_3) = z_3, \tag{11}$$

$$f_2(z_2, z_3) = z_2 + z_3,\ f_3(z_2, z_3) = z_3, \tag{12}$$

$$f_2(z_2, z_3) = z_2 + z_3,\ f_3(z_2, z_3) = z_3/(z_2 + z_3). \tag{13}$$

Note that with the advection functions (11), the system of advection equations (7) is the system of advection equations (3).

With the MINMOD limiter, the reconstructed values at the interface between i-cell and $(i + 1)$-cell of a uniform grid are given as:

$$f_{j,i+1/2} = f_{j,i} + \frac{\phi(r_j)\left(f_{j,i+1} - f_{j,i}\right)}{2}, \tag{14a}$$

$$r_j = \frac{f_{j,i} - f_{j,i-1}}{f_{j,i+1} - f_{j,i}}, \tag{14b}$$

$$\phi\left(r_j\right)=\begin{cases}0, & r_j \le 0.\\ r_j, & 0 < r_j \le 1.\\ 1, & otherwise.\end{cases} \tag{14c}$$

The limiting values $f_{2,i+1/2}$ and $f_{3,i+1/2}$ can have 9 combinations depending on the values of r_2, r_3. Here, we only consider the situation $0 < r_2, r_3 \le 1$ that will be enough to reveal the problem. We analyze the three sets of advection functions one by one.

(1) The advection functions (11) are used with initial values satisfying $f_{2,i} + f_{3,i} < 1,\ 0 < f_{2,i} < 1,\ 0 < f_{3,i} < 1$. The sum of the reconstructed values at the interface $i + 1/2$ is

$$f_{2,i+1/2} + f_{3,i+1/2} = \frac{\left(3f_{2,i} - f_{2,i-1}\right) + \left(3f_{3,i} - f_{3,i-1}\right)}{2}. \tag{15}$$

The value of $(f_{2,i+1/2} + f_{3,i+1/2})$ can be larger than 1. For example, when $f_{2,i-1} = 0.12,\ f_{2,i} = 0.40,\ f_{2,i+1} = 0.70,\ f_{3,i-1} = 0.60,\ f_{3,i} = 0.58,\ f_{3,i+1} = 0.10$, the reconstructed values are $f_{2,i+1/2} = 0.54$ and $f_{3,i+1/2} = 0.57$, sum of which exceeds the upper limit and the condition (5) is violated.

(2) The advection functions (12) are used with initial values satisfying $1 > f_{2,i} > f_{3,i} > 0$. The difference between the reconstructed values at the interface $i + 1/2$ is

$$z_{2,i+1/2} = f_{2,i+1/2} - f_{3,i+1/2} = \frac{3\Delta_i - \Delta_{i-1}}{2},\quad \Delta_i = f_{2,i} - f_{3,i}. \tag{16}$$

The value of $z_{2,i+1/2}$ can be less than 0. For example, when $f_{2,i-1} = 0.40,\ f_{2,i} = 0.50,\ f_{2,i+1} = 0.90,\ f_{3,i-1} = 0.05,\ f_{3,i} = 0.40,\ f_{3,i+1} = 0.80$, the reconstructed values are $f_{2,i+1/2} = 0.55$ and $f_{3,i+1/2} = 0.575$, which means that the condition (4) is violated.

(3) The advection functions (13) are used with initial values $0 < f_{j,i} < 1$. Since the MINMOD limiter does not create new extrema, for the reconstructed values the condition $0 < f_{j,i+1/2} < 1$ still holds. Thus, we have

$$0 < f_{2,i+1/2} = z_{2,i+1/2} + z_{3,i+1/2} < 1,\quad 0 < f_{3,i+1/2} = \frac{z_{3,i+1/2}}{z_{2,i+1/2} + z_{3,i+1/2}} < 1. \tag{17}$$

In this case, the conditions (4) and (5) are obviously kept when the non-linear reconstruction is applied to the advection functions.

One can easily extend Eq. (13) for the N components and choose $N - 1$ independent advection functions $f_2, f_3, \ldots, f_N$ in the form of rational functions as follows:

$$f_j = \frac{\sum_{k=j}^{N} z_k}{\sum_{k=j-1}^{N} z_k},\quad j \in \Psi. \tag{18}$$

Remark 1 The advection function f_j can be interpreted as the bulk volume fraction of j-th, $(j+1)$-th, ..., N-th components in the mixture of $(j-1)$-th, j-th, ..., N-th components.

Remark 2 The rational advection functions (18) may attain singularity if the $(j-1)$-th, ..., N-th components are vanished (i.e., $\sum_{k=j-1}^{N} z_k = 0$). To regularize advection functions (18) we may allow impurity when assigning initial volume fractions. For example, suppose that at some spatial point $M (M \in \mathbb{N}^+$ and $M < N)$ components are vanished, we assume that they exist in a negligible volume fraction $z'_j > 0$ and $\sum_{j\in\Pi} z'_j = \chi$, where Π is

the set containing the indexes of the vanished components. All the other volume fractions decrease by $\chi/(N-M)$ so that $\sum_i^N z_i = 1$ is maintained. According to our numerical tests, χ can be taken as small as 10^{-15}, the order of machine zero. In the present paper, we are interested in the multi-material problems where only gas, liquid and solid explosives are involved. In these problems, the typical maximum density ratio is $10^3 - 10^4$. Therefore, the impurity results in only negligible error in density. In fact, this is an assumption used in the Baer–Nunziato model [3] and its variants. This is also a common numerical practice in the multi-fluid flow modeling and justified against various problems [2,9,24,48,51,52,60]. We will use this method to regularize advection functions (18) in this present work. Methods to deal with this singularity are to be developed in our future work.

Remark 3 Definition of the volume fractions of the vanished components z_j' is important. The simplest definition is $z_j' = \chi/M$, i.e., every component has the same volume fraction. When dealing with discontinuities in volume fraction, we can define z_j' so that the discontinuity in f_j would be minimized.

For example, assume we have the following discontinuity: $(z_1, z_2, z_3) = (\alpha_1\chi, \alpha_2\chi, 1-\chi)$, $x < 0$; $(z_1, z_2, z_3) = (1-\chi, \alpha_2\chi, \alpha_3\chi)$, $x > 0$, where $\alpha_1 + \alpha_2 = 1$ and $\alpha_2 + \alpha_3 = 1$. Thus, we have $(f_2, f_3) = \left(1-(1-\alpha_2)\chi, \frac{1-\chi}{1-(1-\alpha_2)\chi}\right)$ $x < 0$; $(f_2, f_3) = \left((\alpha_2+\alpha_3)\chi, \frac{\alpha_3}{\alpha_2+\alpha_3}\right)$, $x > 0$. Since $\chi \to 0$, we deduce $f_3 \to 1$ for $x < 0$. To minimize the discontinuity in f_3, we want $f_3 = \frac{\alpha_3}{\alpha_2+\alpha_3} \to 1$, which can be achieved by defining α_2 and α_3 such that $\alpha_2 \ll \alpha_3$.

Volume fractions z_j can be recovered from Eq. (18) in the following way:

$$z_j = \begin{cases} \prod_{k=2}^{j} f_k - \prod_{k=2}^{j+1} f_k, & j < N. \\ \prod_{k=2}^{N} f_k, & otherwise. \end{cases} \tag{19}$$

Proposition 1 *If a monotonicity-preserving reconstruction scheme is applied to advection functions in the form of Eq.* (18)*, then given cell average values of volume fractions satisfying conditions* (4) *and* (5)*, the reconstructed volume fractions on cell faces also satisfy conditions* (4) *and* (5)*.*

Proof Since the cell average values of volume fractions $z_{j,i}$ satisfy conditions (4) and (5), we deduce that the cell average values of advection functions (18) satisfy

$$f_{j,i} \in [0, 1], \tag{20}$$

When a monotonicity-preserving reconstruction scheme is applied to these advection functions, no new extrema will be created, which means

$$f_{j,i}^{cf} \in [0, 1], \tag{21}$$

where the superscript "cf" represent the reconstructed values on the cell face.

By using Eq. (18), we further obtain

$$f_{j,i}^{cf} = \frac{\sum_{k=j}^{N} z_{k,i}^{cf}}{\sum_{k=j-1}^{N} z_{k,i}^{cf}} \in [0, 1], \quad j \in \Psi. \tag{22}$$

From Equation (22) we deduce

$$0 \le z_{N,i}^{cf} \le \sum_{k=N-1}^{N} z_{k,i}^{cf} \le \cdots \le \sum_{k=2}^{N} z_{k,i}^{cf} \le \sum_{k=1}^{N} z_{k,i}^{cf} = 1. \tag{23}$$

The inequality (23) ensures that the reconstructed volume fractions satisfy the conditions (4) and (5). □

Since the advection functions (18) are non-linear combinations of volume fractions, monotonicity of advection functions f_j does not ensure monotonicity of volume fractions z_j. However, as shown in the following two propositions, the total variation of volume fractions $TV(z_j)$ has the upper limit that decreases with time.

Proposition 2 *The total variation of the product of two advection functions does not exceed the sum of total variations of advection functions:*

$$TV\left(f_m f_l\right) \leq TV\left(f_m\right) + TV\left(f_l\right). \tag{24}$$

Proof

$$\begin{aligned} TV(f_l f_m) &= \sum_i |(f_l f_m)_{i+1} - (f_l f_m)_i| \\ &= \sum_i |(f_l)_{i+1}[(f_m)_{i+1} - (f_m)_i] + (f_m)_i[(f_l)_{i+1} - (f_l)_i]| \\ &\leq \sum_i |(f_l)_{i+1}[(f_m)_{i+1} - (f_m)_i]| + \sum_i |(f_m)_i[(f_l)_{i+1} - (f_l)_i]|. \end{aligned} \tag{25}$$

Since $0 \leq (f_l)_{i+1}, (f_m)_i \leq 1$, we deduce

$$\begin{aligned} TV(f_l f_m) &\leq \sum_i |(f_l)_{i+1}[(f_m)_{i+1} - (f_m)_i]| + \sum_i |(f_m)_i[(f_l)_{i+1} - (f_l)_i]| \\ &\leq \sum_i |(f_m)_{i+1} - (f_m)_i| + \sum_i |(f_l)_{i+1} - (f_l)_i| \\ &= TV(f_l) + TV(f_m). \end{aligned} \tag{26}$$

□

Proposition 3 *If a monotonicity-preserving scheme is applied to the advection function* (18)*, the total variation of the volume fraction z_j is constrained by the following condition*

$$TV(z_j) \leq C_j, \quad C_j^{n+1} \leq C_j^n. \tag{27}$$

Proof Since the monotonicity-preserving scheme is applied to advection functions, we obtain

$$[TV(f_j)]^{n+1} \leq [TV(f_j)]^n. \tag{28}$$

By using Proposition 2 and Eq. (28), we obtain

$$\begin{cases} TV(z_j) \leq \sum_{k=2}^{j} TV(f_k) + \sum_{k=2}^{j+1} TV(f_k) = C_j, & j < N, \\ TV(z_N) \leq \sum_{k=2}^{N} TV(f_k) = C_N, & otherwise. \end{cases} \tag{29}$$

Combining Eqs. (28) and (29), we obtain Eq. (27). □

In the following, the property of total variation defined by Eq. (27) is referred to as "weak total variation diminishing (WTVD)".

Note that the set of advection functions (18) is not the only feasible choice. In Eq. (18) the volume fractions $z_j (j \in \Psi)$ are chosen as independent variables, while z_1 is derived from Eq. (2). The variable that is derived from Eq. (2) is hereby termed as "derived variable".

In fact, any volume fraction from z_1 to z_N can be selected as the derived variable, different selections of the derived variable give birth to different advection functions. If the l-indexed ($l > 1$) volume fraction is chosen as the derived volume fraction, then the advection functions take the following form:

$$\widehat{f_j} = \frac{\sum_{k=j}^{N} \widehat{z_k}}{\sum_{k=j-1}^{N} \widehat{z_k}}, \quad j \in \Psi, \quad \widehat{z_k} = \begin{cases} z_l, & k = 1, \\ z_{k-1}, & k \leq l, \\ z_k, & k > l. \end{cases} \tag{30}$$

Due to non-linearity of the advection functions (30), solving the advection equations (7) with different advection functions results in different solutions for volume fractions, i.e., our method is not component order invariant. Suppose we have two different sets of advection functions $\widehat{f_j^{(1)}}$, $\widehat{f_j^{(2)}}$ corresponding to $l = l_1, l = l_2$. Then on a uniform 1D grid with n_c cells the distance between two solutions is

$$d(\widehat{z^{(1)}}, \widehat{z^{(2)}}) = \sum_{i=1}^{n_c} \sum_{j=1}^{N} \left| z_{j,i}^{(1)} - z_{j,i}^{(2)} \right| / (n_c \cdot N) > 0. \tag{31}$$

However, since the advection equations (7) with different advection functions have identical analytical solutions for volume fractions, d must converge to zero as space step Δx tends to zero.

Proposition 4 *If a numerical scheme with an order of accuracy $(\Delta x)^p$ is used to solve the advection equations (7) for advection functions (18) or (30), then the order of accuracy for volume fractions is also $(\Delta x)^p$.*

Proof The order of accuracy for f_k is $(\Delta x)^p$, i.e., $f_k = f_k^{exact} + \Upsilon_k, \Upsilon_k = \mathcal{O}((\Delta x)^p)$. Equation (19) shows, z_j is smooth function of f_k with $\left|\partial z_j / \partial f_k\right| \leq 1$. With the aid of Taylor expansion, we obtain $z_j\left(f_2, \ldots, f_N\right) = z_j\left(f_2^{exact}, \ldots, f_N^{exact}\right) + \sum_{k=2}^{N}\left(\partial z_j / \partial f_k\right) \cdot \Upsilon_k + \mathcal{O}\left((\Delta x)^p\right)$, which means $z_j = z_j^{\text{exact}} + \mathcal{O}\left((\Delta x)^p\right)$. □

Proposition 5 *If a numerical scheme with an order of accuracy $(\Delta x)^p$ is used to solve the advection equations for two differently ordered advection functions $\widehat{f^{(1)}}$ and $\widehat{f^{(2)}}$, then $d(\widehat{z^{(1)}}, \widehat{z^{(2)}}) = \mathcal{O}\left((\Delta x)^p\right)$.*

Proof By using Proposition 4, we obtain $\widehat{z_j^{(1)}} = z_j^{\text{exact}} + \mathcal{O}\left((\Delta x)^p\right)$ and $\widehat{z_j^{(2)}} = z_j^{\text{exact}} + \mathcal{O}\left((\Delta x)^p\right)$. It is obvious that $d(\widehat{z^{(1)}}, \widehat{z^{(2)}}) = \mathcal{O}\left((\Delta x)^p\right)$. □

To conclude this section, we remark that by solving the system of advection equations (7) for f_j instead of the system of advection equations for volume fractions (3), we can limit the interpolated values so that conditions (4) and (5) are satisfied on the cell face. Proposition 1 says that any monotonicity-preserving scheme (for example, TVD schemes) can be implemented in the system (7) with maintaining conditions (4) and (5). By comparison, we conclude that the method of Jaouen [27] is based on flux modification, while our method is based on limiting the interpolated values on cell faces. As is shown in Sect. 5, the limited downwind scheme used by Jaouen [27] can also be coupled with our method. Apart from that, as our numerical tests demonstrate, our method can be integrated into various interface-shapening techniques, including the artificial compression method [22,23], the anti-diffusion method [57] and the THINC method [62]. Moreover, our method is much simpler and more general than the method of Jaouen [27].

3 $(2N+1)$-Equation Model for Multi-fluid Flows

In this section, we introduce a $(2N+1)$-equation model for multi-fluid flows of N ($N \geq 3$) components based on the five-equation model [2]. The numerical method proposed in Sect. 2 is integrated into this model to ensure conditions (4) and (5).

3.1 Definition of the Model

The $(2N+1)$-equation model considered is written as follows:

$$\begin{cases} \partial z_i \rho_i / \partial t + \operatorname{div}(z_i \rho_i \mathbf{u}) = 0, \quad i \in \Phi, \\ \partial \rho \mathbf{u} / \partial t + \operatorname{div}(\rho \mathbf{u} \otimes \mathbf{u} + P \mathbf{I}_d) = 0, \\ \partial \rho e / \partial t + \operatorname{div}(\rho H \mathbf{u}) = 0, \\ \partial f_j / \partial t + \mathbf{u} \cdot \operatorname{grad} f_j = 0, \quad j \in \Psi. \end{cases} \tag{32}$$

where we define the following mixture variables: density $\rho = \sum_{i=1}^{N} (z_i \rho_i)$, specific internal energy $\varepsilon = \sum_{i=1}^{N} (z_i \rho_i \varepsilon_i) / \rho$, specific enthalpy $h = \sum_{i=1}^{N} (z_i \rho_i h_i) / \rho$, specific total energy $e = \varepsilon + |\mathbf{u}|^2/2$, specific total enthalpy $H = e + P/\rho$.

The mixture acoustic velocity in this model is defined as:

$$\zeta c^2 = \sum_{i=1}^{N} \rho_i z_i \zeta_i c_i^2 / \rho, \quad \zeta_i = \partial \rho_i \varepsilon_i / \left. \partial P_i \right|_{\rho_i}, \quad \zeta = \sum_{i=1}^{N} z_i \zeta_i \tag{33}$$

where c and c_i are the sound velocity of the mixture and i-th component, respectively.

There are $2N+1$ equations (in 1D, or $2N+3$ equations in 3D) and $3N$ variables (in 1D, or $3N+2$ variables in 3D), which are $z_2, \ldots, z_N, \rho_1, \rho_2, \ldots, \rho_N, \mathbf{u}, \varepsilon_1, \varepsilon_2, \ldots, \varepsilon_N$. The model is not closed, and closure relations and the mixture equation of state are to be determined below.

One can see that the five-equation model of Allaire et al. [2] is a particular case of our $(2N+1)$-equation model when $N = 2$ and $f_2(z_2) = z_2$. Our model is not direct generalization of the five-equation model. The advection functions are not volume functions; rather they are properly defined functions of volume fractions ensuring existence of stable and physically admissible solutions.

Remark 4 The model (32) is temperature non-equilibrium by allowing N temperatures. Here, it is assumed that the thermal relaxation occurs too slowly to be relevant on the time scale of interest. This assumption is admissible for a certain scope of problems when the heat exchange rate is small with respect to the time scale of the problem solved (see analysis in [30]).

Remark 5 The essence of this numerical model lies in replacing the advection equations for volume fractions with those for the proposed advection functions. Therefore, this method can also be used with more complicated models, such as the reduced five-equation model [30], six-equation model [48], and the seven-equation model [46] with different physical processes. Surface tension and viscous effects have already been implemented by the authors [63]. For the sake of clarity, we only focus on the model (32) in the present work.

3.2 Equation of State

To describe different material properties, we use the EOS in the form of generalized Van der Waals equation [2,54], which is written as

$$P_i(\rho_i, \rho_i\varepsilon_i) = \left(\frac{\gamma_i - 1}{1 - b_i\rho_i}\right)(\rho_i\varepsilon_i - \pi_i + a_i\rho_i^2) - (\pi_i + a_i\rho_i^2), \tag{34}$$

where γ is the ratio of specific heats; a is a constant accounting for the attraction between molecules; b is a constant accounting for the volume that a real gas molecule has; π is a pressure-like constant that can be obtained by fitting experimental data.

The Mie–Gruneisen EOS is also widely used for characterizing different materials in simulations of multi-material flows and is written as

$$P_i(\rho_i, \rho_i\varepsilon_i) = [\gamma_i(\rho_i) - 1]\rho_i\varepsilon_i - \gamma_i(\rho_i)\pi_i(\rho_i). \tag{35}$$

The Mie–Gruneisen EOS (35) is more general than the Van der Waals EOS (34). It can characterize various gaseous or solid explosives, and solid metals under high pressure. Note that the generalized Van der Waals EOS can be viewed as a case of the Mie–Gruneisen EOS.

Both the EOSs (34) and (35) can be written in the following unique form:

$$P_i(\rho_i, \rho_i\varepsilon_i) = G_i(\rho_i)\rho_i\varepsilon_i - H_i(\rho_i). \tag{36}$$

Here we assume that $G_i(\rho_i) > 0$ for each component, which is met for most materials [2,21,54]. Moreover, we assume that the sound velocity of the material defined by EOS (36) is real, which is ensured by the following relation

$$\left(h_i - \left(\frac{\partial\rho_i\varepsilon_i}{\partial\rho_i}\right)|_P\right) G_i(\rho_i) > 0. \tag{37}$$

3.3 Consistency

To close the system (32), we use the isobaric closure:

$$P = P_1(\rho_1, \rho_1\varepsilon_1) = P_2(\rho_2, \rho_2\varepsilon_2) = \cdots = P_N(\rho_N, \rho_N\varepsilon_N). \tag{38}$$

With the condition for mixture internal energy, Eq. (38) yields the following system of equations

$$\begin{cases} P_1(\rho_1, \rho_1\varepsilon_1) = P_j(\rho_j, \rho_j\varepsilon_j) = P, \quad j \in \Psi, \\ z_1\rho_1\varepsilon_1 + z_2\rho_2\varepsilon_2 + \cdots + z_N\rho_N\varepsilon_N = \rho\varepsilon. \end{cases} \tag{39}$$

To guarantee that the conserved variables $z_1\rho_1, \ldots, z_N\rho_N, \rho\mathbf{u}, \rho e, f_2, \ldots, f_N$ uniquely define non-conservative variables $\rho_1, \ldots, \rho_N, \mathbf{u}, \varepsilon_1, \varepsilon_2, \ldots, \varepsilon_N, z_2, \ldots, z_N$, it is necessary to prove that the system (39) has unique solution $(\rho_1\varepsilon_1, \rho_2\varepsilon_2, \ldots, \rho_1\varepsilon_N)$. This property is referred to as consistency by Allaire et al. [2].

Proposition 6 *The isobaric closure Eq.* (38) *allows to uniquely recover the pressure P of the model* (32) *when the EOS in the form of Eq.* (36) *is used.*

Proof The variables $\rho\varepsilon, z_1\rho_1, z_2\rho_2, \ldots, z_N\rho_N, f_2, f_3, \ldots, f_N$ can be obtained by solving the system (32). Moreover, the volume fractions $z_1, z_2, \ldots, z_N$ can be uniquely recovered from $f_2, f_3, \ldots, f_N$. Having obtained z_j, one can further calculate ρ_j. These variables are assumed to be known here.

We define N variables $x_i : x_i = z_i\rho_i\varepsilon_i/\rho\varepsilon, i \in \Phi$. By using the definition of x_i and substituting Eq. (36) into the system (39), we can get the following linear system of equations for $x_1, x_2, \ldots, x_N$:

$$\frac{G_1(\rho_1)\rho\varepsilon}{z_1}x_1 - \frac{G_j(\rho_j)\rho\varepsilon}{z_j}x_j = H_j(\rho_j) - H_1(\rho_1),\ j \in \Psi, \quad \sum_i^N x_i = 1. \tag{40}$$

The corresponding determinant is

$$D = \frac{(\rho\varepsilon)^{N-1}\sum_{i=1}^N (z_i \prod_{k=1,k\neq i}^N G_k(\rho_k))}{\prod_{i=1}^N z_i}. \tag{41}$$

Based on the assumption on the EOS (36), we obtain $D \neq 0$, which can lead us to the conclusion that the system (40) has only one solution $(x_1, x_2, \ldots, x_N)$.

Furthermore, the solution can be expressed as

$$x_i = \frac{z_i/G_i(\rho_i)}{\sum_{i=1}^N z_i/G_i(\rho_i)} \in (0, 1). \tag{42}$$

Therefore, the pressure P is uniquely determined. □

With the isobaric closure, we obtain the EOS for the mixture,

$$P(\rho_1, \rho_2, \ldots, \rho_N, \rho\varepsilon, z_1, z_2, \ldots, z_N) = \left[\sum_i^N \frac{z_i}{G_i(\rho_i)}\right]^{-1}\left[\rho\varepsilon + \sum_i^N \frac{z_i H_i(\rho_i)}{G_i(\rho_i)}\right]. \tag{43}$$

3.4 Evolution of the Constant-Pressure Profile

In order to avoid spurious oscillations in pressure and velocity, the model of (3.1) should ensure the PV property—keeping constant pressure and velocity distributions. To meet this property, some restrictions should be imposed on the advection function. We first consider the situation when only three components exist and then generalize the result to the situation of $N(N > 3)$ components. We perform analysis of the pure advection problem, where only the advection functions are varied with the spatial coordinate in the initial data. We consider Riemann solvers which are accurate on isolated contact discontinuity, such as the Roe solver and the HLLC solver with the above-mentioned isobaric closure. The exact solution is the advection of z_i profiles with the constant velocity.

Here, we introduce the state vector

$$\mathbf{Q}^K = \left[\rho_1^K \quad \rho_2^K \quad \rho_3^K \quad u^K \quad P^K \quad f_2^K \quad f_3^K\right],$$

where $K = L, R, *$, which represent the state on the left side of $x = 0$, on the right side of $x = 0$, and the state of the $[0, \Delta x]$ cell after one time step Δt, respectively, and consider the pure advection problem with initial data: $u^L = u^R = u > 0$, $\rho_i^L = \rho_i^R = \rho_i, \varepsilon_i^L = \varepsilon_i^R = \varepsilon_i$, $f_j^L \neq f_j^R, i = 1, 2, 3, j = 2, 3$.

Proposition 7 *In order to ensure constant pressure profile in the above advection problem, the advection functions $f_j(z_2, z_3)$ must be linear with respect to z_2, z_3:*

$$f_j(z_2, z_3) = A_j z_2 + B_j z_3, \quad j = 2, 3, \tag{44}$$

where A_j and B_j are constants.

Proof Since the velocity $u > 0$, the updated state can be obtained with

$$\begin{cases} \rho_i^* z_i^* = u\lambda \rho_i^L z_i^L + (1-u\lambda)\rho_i^R z_i^R, \quad i = 1, 2, 3, \\ \rho^* u^* = u\lambda \rho^L u^L + (1-u\lambda)\rho^R u^R, \\ \rho^* e^* = u\lambda \rho^L e^L + (1-u\lambda)\rho^R e^R, \\ f_j^* = u\lambda f_j^L + (1-u\lambda) f_j^R, \quad j = 2, 3. \end{cases} \tag{45}$$

According to the proof of Allaire et al. [2], if

$$z_2^* = u\lambda z_2^L + (1-u\lambda) z_2^R, \tag{46a}$$

$$z_3^* = u\lambda z_3^L + (1-u\lambda) z_3^R, \tag{46b}$$

the constant pressure profile condition is satisfied.
Sufficiency If Eq. (44) is valid, from the last equation of the system of equations (45) and after some algebraic manipulations we obtain

$$\begin{cases} A_2 \left[z_2^* - u\lambda z_2^L - (1-u\lambda) z_2^R \right] + B_2 \left[z_3^* - u\lambda z_3^L - (1-u\lambda) z_3^R \right] = 0, \\ A_3 \left[z_2^* - u\lambda z_2^L - (1-u\lambda) z_2^R \right] + B_3 \left[z_3^* - u\lambda z_3^L - (1-u\lambda) z_3^R \right] = 0. \end{cases} \tag{47}$$

If we treat the parts in square brackets as unknowns, and based on Eq. (8), we get the Eq. (46).
Necessity Let us assume that

$$f_j(z_2, z_3) = \left[A_j(z_2, z_3) \right] z_2 + \left[B_j(z_2, z_3) \right] z_3, \quad j = 2, 3. \tag{48}$$

Then the updated value for f_j is

$$\begin{aligned} f_j\left(z_2^*, z_3^*\right) &= \left[A_j\left(z_2^*, z_3^*\right) \right] z_2^* + \left[B_j\left(z_2^*, z_3^*\right) \right] z_3^* \\ &= u\lambda \left\{ \left[A_j\left(z_2^L, z_3^L\right) \right] z_2^L + \left[B_j\left(z_2^L, z_3^L\right) \right] z_3^L \right\} \\ &\quad + (1-u\lambda) \left\{ \left[A_j\left(z_2^R, z_3^R\right) \right] z_2^R + \left[B_j\left(z_2^R, z_3^R\right) \right] z_3^R \right\}. \end{aligned} \tag{49}$$

Subtracting $[A_j\left(z_2^*, z_3^*\right) \times Eq.\,(46a) + B_j\left(z_2^*, z_3^*\right) \times Eq.\,(46b)]$ from Eq. (49), one finds that

$$\begin{aligned} &\left[A_j\left(z_2^L, z_3^L\right) - A_j\left(z_2^*, z_3^*\right) \right] u\lambda z_2^L + \left[A_j\left(z_2^R, z_3^R\right) - A_j\left(z_2^*, z_3^*\right) \right] (1-u\lambda) z_2^R \\ &+ \left[B_j\left(z_2^L, z_3^L\right) - B_j\left(z_2^*, z_3^*\right) \right] u\lambda z_3^L + \left[B_j\left(z_2^R, z_3^R\right) - B_j\left(z_2^*, z_3^*\right) \right] (1-u\lambda) z_3^R = 0. \end{aligned} \tag{50}$$

Since $z_2^L, z_2^R, z_3^L, z_3^R$ are arbitrary in [0, 1], we get

$$\begin{cases} A_j\left(z_2^*, z_3^*\right) = A_j\left(z_2^L, z_3^L\right) = A_j\left(z_2^R, z_3^R\right), \\ B_j\left(z_2^*, z_3^*\right) = B_j\left(z_2^L, z_3^L\right) = B_j\left(z_2^R, z_3^R\right). \end{cases} \tag{51}$$

Again from the fact that $z_2^L, z_2^R, z_3^L, z_3^R$ can take arbitrary values in [0, 1], we deduce that A_j and B_j must be constants. □

The proposition still holds for the situation of $N (N > 3)$ components, which can be proved analogously.

According to Proposition 7, for N components, the advection functions for updating are taken as:

$$f_j = \sum_{k=j}^{N} z_k, \quad j \in \Psi. \tag{52}$$

Remark 6 The other advection functions in the form of linear combinations of volume fractions are also possible and maintain the PV property.

According to Proposition 7, rational functions (30) that we defined to ensure non-negativity do not satisfy the constant pressure condition. Here, we discuss possible schemes that settle the contradiction in the definition of the advection functions imposed by the non-negativity and PV properties.

Scheme A Use different advection functions for reconstruction and updating: rational functions (18) or (30) for reconstruction and linear functions (52) for updating.

Scheme B Instead of Eq. (32), we solve the following system of equations

$$\begin{cases} \partial z_i \rho_i / \partial t + \operatorname{div}(z_i \rho_i \mathbf{u}) = 0, & i \in \Phi, \\ \partial \rho \mathbf{u} / \partial t + \operatorname{div}(\rho \mathbf{u} \otimes \mathbf{u} + P \mathbf{I}_d) = 0, & \\ \partial \rho e / \partial t + \operatorname{div}(\rho H \mathbf{u}) = 0, & \\ \partial f_{ja}^{lin} / \partial t + \mathbf{u} \cdot \operatorname{grad} f_j^{lin} = 0, & j \in \Psi, \\ \partial f_j^{ra} / \partial t + \mathbf{u} \cdot \operatorname{grad} f_j^{ra} = 0, & j \in \Psi. \end{cases} \tag{53}$$

The solution procedures for the system of Eq. (53) are as follows:

Step 1 With the last two advection equations for the linear advection functions f_j^{lin} and the rational ones f_j^{ra}, we obtain two different sets of volume fractions: $z_j^{lin} = z_j\left(f_2^{lin}, f_3^{lin}, \ldots, f_N^{lin}\right)$ and $z_j^{ra} = z_j\left(f_2^{ra}, f_3^{ra}, \ldots, f_N^{ra}\right)$. Note that when solving the advection equations for f_j^{lin}, in order to ensure the non-negativity conditions we adopt the same strategy as that in Scheme A: perform reconstruction with the rational adevction functions.

Step 2 z_j^{lin} is used for calculating the primitive variables (pressure P, velocity $\mathbf{u}$ and density ρ_i) for the sake of the PV property.

Step 3 z_j^{lin} is corrected to z_j^{ra} without modifying velocity, pressure and entropy of each phase as in [60].

Remark 7 The solutions of these two sets of advection equations converge to the same analytical solutions for volume fractions. According to the results of our numerical tests, in the case of smooth z_j profile the distance between their solutions is of the order of 10^{-15} (see Sect. 5.2).

Proposition 8 *If TVD schemes are used to solve Eq. (53) following the solution procedures of Scheme B, then the WTVD property is ensured for the cell-averaged volume fractions.*

Proof According to the solution procedures of Scheme B, we conclude that the cell-averaged volume fractions are totally defined by the cell-averaged rational advection functions. By using Proposition 3, we obtain Proposition 8. □

Remark 8 For Scheme A, the inconsistency between advection functions in the reconstruction and updating procedures may formally invalidate Proposition 3, nevertheless, our numerical tests demonstrate that Scheme A has a TVD property comparable to Scheme B. In

fact, this kind of inconsistency is also observed in the conventional FVM for gas dynamics where the conserved variables are used for updating the cell-averaged state while the primitive/characteristic variables for interpolating.

4 Numerical Method

In this section, we deal with the numerical method for solving the governing equations of the multi-fluid flow model considered above. We will apply the FVM to perform the discretization in space. The interface-sharpening method THINC [56,62] is applied to reduce the numerical smearing of the material interfaces.

4.1 Numerical Flux

We assume that the computational grid consists of non-overlapping polyhedrons and does not change in time. The spatial discretization is performed with the FVM and the explicit time marching scheme is adopted. On the interface σ of a cell i, the following unit vectors form a local orthonormalized basis in $\mathbb{R}^3$: $\mathbf{n}$—the outward normal to the interface σ; $\mathbf{l}$, $\mathbf{k}$—the tangential vectors to the interface σ. In the local coordinate system, one has the local velocities along each coordinate: u_n, u_k, u_l.

The conservative state vector in a Cartesian system of coordinates is

$$\mathbf{q} = \left[z_1\rho_1 \;\; z_2\rho \;\; \ldots \;\; z_N\rho_N \;\; \rho u_1 \;\; \rho u_2 \;\; \rho u_3 \;\; \rho e\right],$$

and the corresponding flux is

$$\mathbf{F}(\mathbf{q}) = \left[z_1\rho_1 u_1 \;\; z_2\rho_2 u_1 \;\; \cdots \;\; z_N\rho_N u_1 \;\; \rho {u_1}^2 + P \;\; \rho u_1 u_2 \;\; \rho u_1 u_3 \;\; \rho H u_1\right].$$

The FVM discretization results in the following equation:

$$\mathbf{q}_i^{n+1} = \mathbf{q}_i^n - \frac{\Delta t}{V_i}\sum_{\sigma} {\mathbf{T}_\sigma}^{-1}\mathbf{F}_\sigma S_\sigma, \tag{54}$$

where V_i is the volume of the i-cell, S_σ is the area of the cell face σ.

The vector $\mathbf{F}_\sigma$ is the locally one-dimensional interface flux in the direction of the outward normal $\mathbf{n}$ which has the following form:

$$\begin{aligned}\mathbf{F}_\sigma &= \mathbf{F}(\mathbf{T}_\sigma \cdot \mathbf{q})\\ &= \left[z_1\rho_1 u_n \;\; z_2\rho_2 u_n \;\; \cdots \;\; z_N\rho_N u_n \;\; \rho {u_n}^2 + P \;\; \rho u_n u_l \;\; \rho u_n u_k \;\; (\rho e + P)\, u_n\right].\end{aligned} \tag{55}$$

In the above formulas, $\mathbf{T}_\sigma$ is the rotation matrix from the absolute coordinate system to the local coordinate system related to the cell face.

In the present paper, two approximate Riemann solvers are utilized for flux approximation: (1) the Roe-type scheme and (2) the HLLC scheme [9,61]. The Roe-type scheme for our model is obtained by generalizing the method designed for two components in [2].

4.2 Interface-Sharpening

The THINC method [56,62] is used for the reconstruction of the sub-grid discontinuity of the advection function at each cell edge. The THINC method uses the hyperbolic tangent function to reconstruct the distribution of advection functions. This scheme belongs to the

type of TVD schemes because it creates no new extrema. Hence, advection functions (18) ensure the conditions (4) and (5) during the reconstruction procedure. After reconstructing advection functions, we can calculate corresponding new volume fractions. The sharpening algorithm is applied only to the numerical transition zone of diffuse interfaces which can be located by the following conditions:

$$\left(f_{j,i+1} - f_{j,i}\right) \cdot \left(f_{j,i} - f_{j,i-1}\right) > 0, \quad \chi < f_{j,i} < 1 - \chi, \tag{56}$$

where χ is a small threshold (for example, 10^{-8}).

4.3 Algorithm

The algorithm for Scheme B consists of the following steps:

(1) Reconstruct the primitive variables at cell faces of each cell by using the cell averaged primitive variables $\mathbf{Q}_{av,pr} = \left[z_i \rho_i, \mathbf{u}, P, f_j^{ra}\right], i \in \Phi, j \in \Psi$ at the time level t^n with the standard MUSCL to obtain the primitive variable vector at the cell face $\mathbf{Q}_{cf,pr}$.
(2) Apply the THINC sharpening scheme to the rational advection functions f_j^{ra} where the condition (56) is satisfied and obtain their sharpened values at the cell face $f_j^{ra,s}$, compute the sharpened volume fractions z_j^s at the cell faces from $f_j^{ra,s}$.
(3) Replace the advection functions f_j^{ra} in $\mathbf{Q}_{cf,pr}$ with $f_j^{ra,s}$, obtain the corresponding conserved variable vector at cell faces $\mathbf{Q}_{cf} = \left[z_i^s \rho_i, \rho\mathbf{u}, \rho e, f_j^{lin,s}, f_j^{ra,s}\right]$, where $f_j^{lin,s} = f_j^{lin}\left(z_2^s, \ldots, z_N^s\right)$.
(4) Compute the numerical flux with the Roe-type or HLLC scheme by using cell face state Q_{cf}.
(5) Integrate cell average values with time to obtain new cell averages $[\rho_i z_i, \rho\mathbf{u}, \rho e, f_j^{lin}, f_j^{ra}]$ at the time level t^{n+1}, and calculate z_j^{lin} and z_j^{ra} from obtained f_j^{lin} and f_j^{ra}, respectively. The primitive variables $\rho_i, \mathbf{u}, P$ are recovered by using z_j^{lin}.
(6) $\mathbf{Q}_{av,pr}^{ra} = \left[\rho_i, \mathbf{u}, P, f_j^{lin}\left(z_2^{ra}, \ldots, z_N^{ra}\right), f_j^{ra}\left(z_2^{ra}, \ldots, z_N^{ra}\right)\right]$ is taken as the updated state at the time level t^{n+1}.

Scheme A differs from Scheme B in two aspects:

First, the rational advection functions f_j^{ra} are only used for reconstruction and the advection equations for f_j^{ra} are not solved. Thus, f_j^{ra} are absent in the state vectors.

Second, in Step (6) $\mathbf{Q}_{av,pr}^{lin} = \left[\rho_i, \mathbf{u}, P, f_j^{lin}\left(z_2^{lin}, z_3^{lin}, \ldots, z_N^{lin}\right)\right]$ is taken as the updated state at time step t^{n+1}.

Remark 9 The above algorithm maintains the pressure-velocity consistency condition. In fact, Step (3) is consistent with the model proposed in [60] where a mathematical regularization is introduced for interface-sharpening.

Remark 10 For non-interfacial cells where the condition (56) is not satisfied, steps (2)–(3) are skipped over and the reconstructed values by the MUSCL scheme are kept.

Remark 11 In fact, Scheme B consist of two step: (1) solution with Scheme A, (2) correction of the volume fraction field. The solution to the additional set of advection equations for

f_j^{ra} serves as a post-processing correction to the volume fraction field to ensure the WTVD property after each time step. This correction does not impact the conservativeness of the scheme.

5 Numerical Tests

In this section, several one-dimension and two-dimension numerical tests with the generalized Van der Waals EOS are performed to validate the proposed numerical method. The MUSCL reconstruction scheme with MINMOD limiter is used for high-order reconstruction and the THINC method is implemented to prevent material interfaces from smearing. If not mentioned, for all numerical tests we use the following default settings: (1) the CFL number is set to be 0.2; (2) the SI unit system is used for all the variables; (3) a uniform regular grid is utilized; (4) we use advection functions (18) for reconstruction; (5) Scheme A is used as a default scheme due to its simplicity and the fact that both schemes have very similar convergence performance, as demonstrated below. The 2D problems are solved with the HLLC method.

5.1 Transport of Seven Materials

To check the effectiveness of our method for the transport of an arbitrary number of materials, we consider the 1D transport problem for seven materials. Here we only solve the advection equations for volume fractions. For comparison purpose, the problem setup is identical with Jaouen et al. [27]. The computational domain is [0, 1]. The initial data is given as:

$$\begin{cases} z_1(x) = \Xi_{[0,1/2]}(x)\,\frac{1+\sin(2\pi x)}{10}, \quad z_2(x) = \left|x - \frac{1}{2}\right|, \\ z_3(x) = \frac{1.5+\sin(0.7+2\pi x)}{14}, \quad z_4(x) = \frac{1}{2}e^{-100(x-1/2)^2}, \\ z_5(x) = \frac{1+\cos(10\pi x)}{14}, \quad z_6(x) = \frac{1}{7}\Xi_{[0.7,1]}(x), \\ z_7(x) = 1 - \sum_{k=1}^{6} z_k(x), \end{cases} \tag{57}$$

where

$$\Xi_I(x) = \begin{cases} 1 - 10^{-8}, & x \in I, \\ 10^{-8}, & x \notin I. \end{cases}$$

The distribution of initial data is illustrated in Fig. 1. Periodical boundary conditions are imposed on both sides of the computational domain. The advection velocity is $u = 1.0$. The numerical scheme is given by Eq. (9). The MUSCL scheme with MINMOD limiter and the limited downwind scheme are tested. With advection functions Eq. (18), we obtain the numerical results on a grid 1000 cells (Fig. 2) after one revolution ($t = 1.0$). We evaluate the convergence of the numerical results with Equation (31). The distance of the numerical results obtained with the MUSCL scheme to the exact solution is 1.38×10^{-3}, while that of the results obtained with the Limited downwind scheme is 6.86×10^{-4}. The non-negativity conditions (4) and (5) are well maintained at every time step.

Figure 3 displays the numerical results for z_1 obtained by directly solving the advection equations for volume fractions Eq. (3) on a 1000-cell grid. Negative values and spurious oscillations are observed.

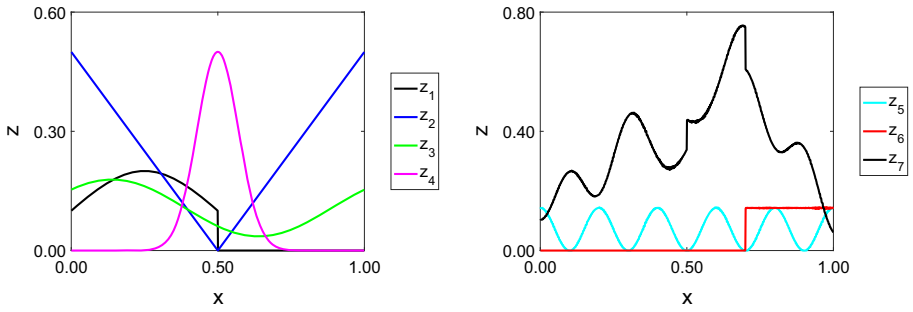

(a) Volume fractions $z_1 - z_4$ **(b)** Volume fractions $z_5 - z_7$

Fig. 1 Initial profile of volume fractions z_1–z_7

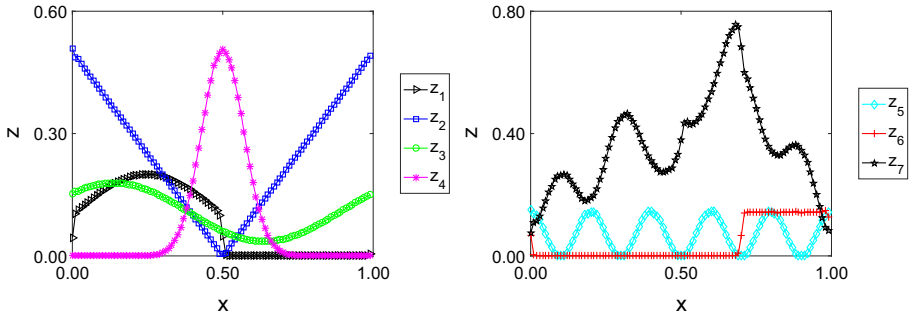

(a) Volume fractions $z_1 - z_4$ **(b)** Volume fractions $z_5 - z_7$

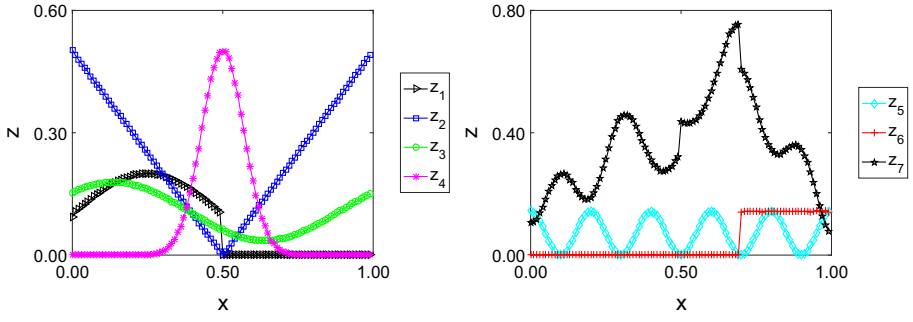

(c) Volume fractions $z_1 - z_4$ **(d)** Volume fractions $z_5 - z_7$

Fig. 2 Numerical results on a 1000-cell grid after one revolution: **a**, **b** obtained with MUSCL scheme; **c**, **d** obtained with the limited downwind scheme. One in every ten points is displayed

5.2 Convergence Test

We investigate the convergence performance of different schemes. Consider the transport of three components in the computational domain [0, 1] with the following initial volume fractions:

$$z_2(x) = \frac{\cos((2x-1)\pi)+1}{4}, \tag{58}$$

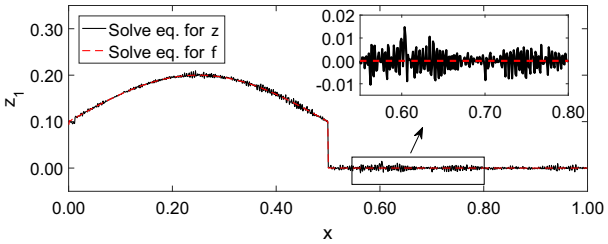

Fig. 3 Numerical results obtained with LD scheme on a 1000-cell grid after one revolution: the solid line—numerical results obtained by directly solving the advection equations for volume fractions, the dashed line—by solving the advection equations for rational advection functions

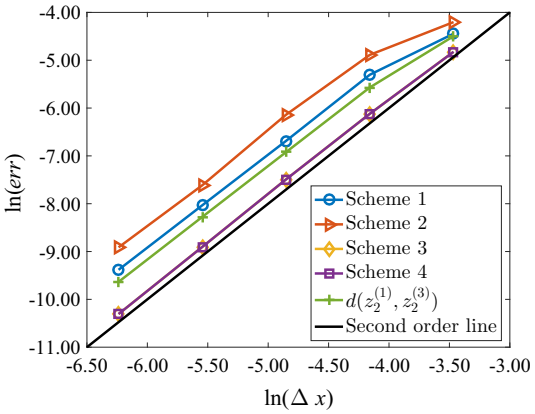

Fig. 4 The convergence performance of different schemes

$$z_3(x) = \frac{\sin((8x-1)\pi/2)+1}{4}, \tag{59}$$

$$z_1(x) = 1 - z_2(x) - z_3(x). \tag{60}$$

The three components are moving to the right with an advection velocity $u = 1.0$. Periodical boundary conditions are imposed on both sides. We test the following schemes:

1. Use advection functions $f_2^{(1)} = z_2 + z_3,\ \ f_3^{(1)} = z_3/(z_2+z_3)$ for reconstruction and updating;
2. Use advection functions $f_2^{(2)} = z_1 + z_2,\ \ f_3^{(2)} = z_2/(z_1+z_2)$ for reconstruction and updating;
3. Use advection functions $f_2^{(3)} = z_1 + z_3,\ \ f_3^{(3)} = z_3/(z_1+z_3)$ for reconstruction and updating;
4. Use advection functions $f_2 = z_1+z_3,\ \ f_3 = z_3/(z_1+z_3)$ for reconstruction, and $z_2,\ z_3$ for updating.

We have performed computations with the above schemes on a series of grids with 32, 64, 128, 256, 512 cells. We use $z_2^{(l)}$ to denote the numerical solution for z_2 obtained with the l-th scheme. The error $err^{(l)}$ is defined as the distance from $z_2^{(l)}$ to the exact solution $z_2^{(ex)}$ in the L^1-space.

The convergence performance of the four schemes at $t = 1.0$ (after one cycle) is demonstrated in Fig. 4. Here we also include the L^1 distance between $z_2^{(1)}$ and $z_2^{(3)}$—$d(z_2^{(1)}, z_2^{(3)})$.

The accuracy orders are as follows: $err^{(1)} = \mathcal{O}(\Delta x^{1.818})$, $err^{(2)} = \mathcal{O}(\Delta x^{1.752})$, $err^{(3)} = \mathcal{O}(\Delta x^{1.983})$, $err^{(4)} = \mathcal{O}(\Delta x^{1.983})$, $d(z_2^{(1)}, z_2^{(3)}) = \mathcal{O}(\Delta x^{1.873})$.

These results verify Propositions 4 and 5.

Scheme 3 and Scheme 4 are in fact Scheme B and Scheme A, respectively. The numerical results of the two schemes are almost the same with a distance of the order 10^{-15}.

5.3 Composite Riemann Problem

We consider the three-material composite Riemann problem. The problem setup is identical to that of Friess et al. [17]. Three different materials are separated by two material interfaces in the 1 m long computational domain. From left to right are the perfect gas 1 ($\gamma = 1.60$), perfect gas 2 ($\gamma = 2.40$) and perfect gas 3 ($\gamma = 1.40$). At the initial moment the gases are in a stationary state and their densities are $\rho_1 = 1.000$, $\rho_2 = 0.125$ and $\rho_3 = 0.100$, respectively. The sub-domains [0.0 m, 0.4 m], [0.4 m, 0.6 m], and [0.6 m, 1.0 m] are filled with the perfect gas 1, 2 and 3 , respectively. The initial pressure is 1.0 in [0.0 m, 0.4m], and 0.1 in other sub-domains. The rational advection used are $f_1 = z_1 + z_2$ and $f_2 = z_2/(z_1 + z_2)$. From the numerical results (Fig. 5) we observe a good agreement between the numerical results and exact solutions for both schemes. No violation of the non-negativity constraints happens throughout the simulation.

5.4 Interface-Shock Interaction

In this section, we perform a more delicate test—interface-shock interaction problem. The test is similar to but more complicated than those in [2]. The materials involved in this test are two stiffened gas materials and a Van der Waals material. Materials properties are displayed in Table 1.

The length of the computational domain is 1.0 m. From left to right are the Van der Waals gas, the stiffened gas material 1, stiffened gas material 2. The interfaces between the materials are initially located at $x = 0.4$ m and $x = 0.5$ m, respectively. Constant boundary conditions are applied on both sides of the computational domain. The stiffened gas material 2 travels from right to left at a speed of 432.69 m/s. The initial pressure is 10^9 Pa in the sub-domain [0.5 m, 1.0 m], and 10^5 Pa in the other sub-domains. The materials on each side of the initial pressure discontinuity are described by different EOSs. The initial densities of each component are taken from Table 1. Computations are performed on a coarse grid (500 cells) and a fine grid (50,000 cells). The numerical results at 270 μ s are displayed in Fig. 6. From these results we can see that the interfaces between three materials are well preserved after long-time evolution.

Furthermore, we compare the numerical results of volume fractions when different variables are used for the reconstruction process. We perform a numerical test on a 100-cells grid with three sets of reconstruction advection functions: advection functions (11), (12) and (13). The results with the Roe-type method after 100 time steps are shown in Fig. 7. As one can see, ReVars 2 causes spurious oscillations in the profile of z_2 and ReVars 1 causes spurious oscillations in the profile of z_1 near the interface between the stiffened gas materials. For these two selections, computations fail after a few steps because they violate positivity constraints and result in spurious oscillations in pressure and producing numerical acoustic disturbances. ReVars 3 ensures non-oscillatory results near the interface since the conditions (4) and (5) are satisfied.

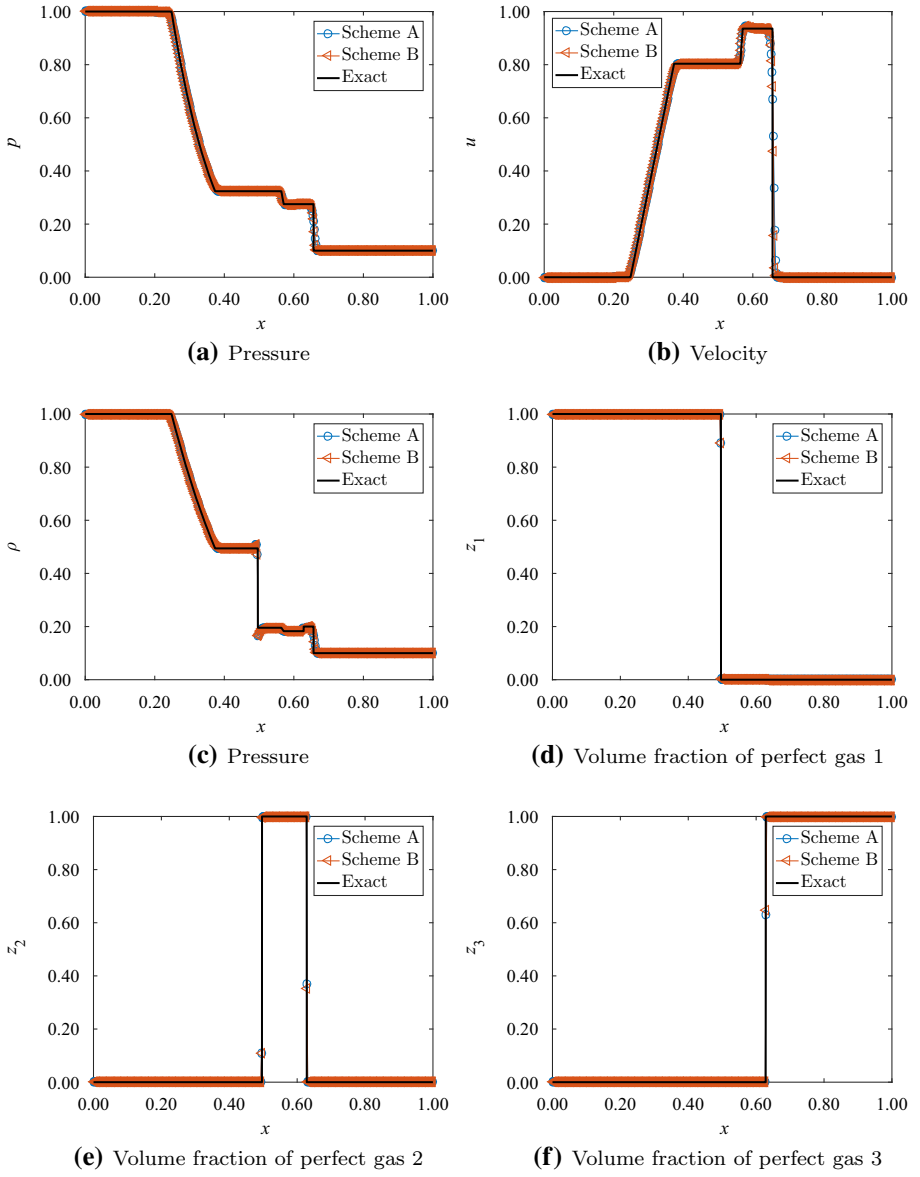

Fig. 5 Numerical results of the composite Riemann problem at the instant 120 μs on a 500-cell grid

Table 1 Material properties for the interface-shock problem

Material	γ	a (Pa m^6/kg)	b (m^3/kg)	π (Pa)	ρ_i (kg/m^3)
Van der Waals gas	1.400	5	10^{-3}	0	1.2
Stiffened gas 1	5.527	0	0	6.146×10^8	1000
Stiffened gas 2	4.400	0	0	6.000×10^8	1230

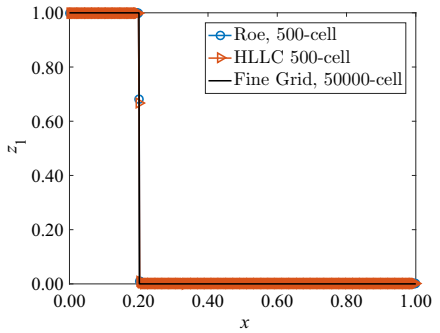

(a) Volume fraction of the Van der Waals gas

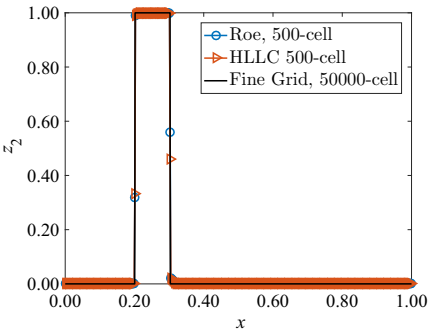

(b) Volume fraction of the stiffened gas 1

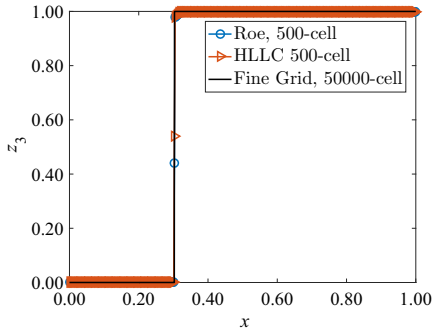

(c) Volume fraction of the stiffened gas 2

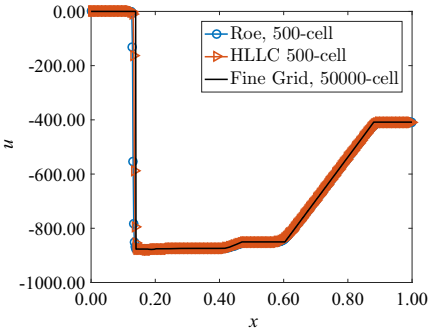

(d) Velocity

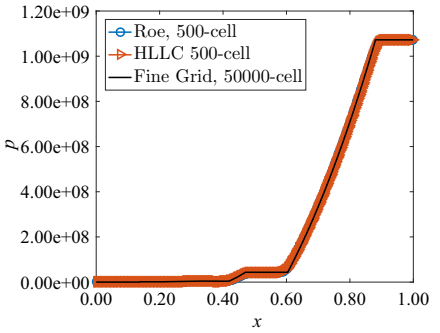

(e) Pressure

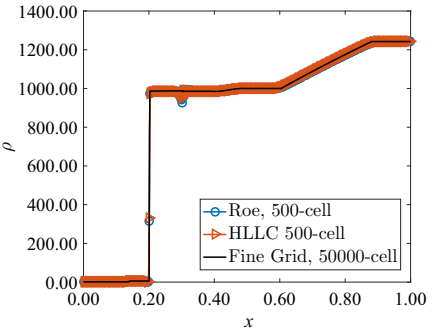

(f) Density

Fig. 6 Numerical results of the interface-shock interaction problem. The black solid line—results on a 5000-cell grid with MUSCL scheme, the green line marked with "∘"—results obtained with the Roe-type method on a 500-cell grid, the red line marked with "▷"—results obtained with the HLLC on a 500-cell grid (Color figure online)

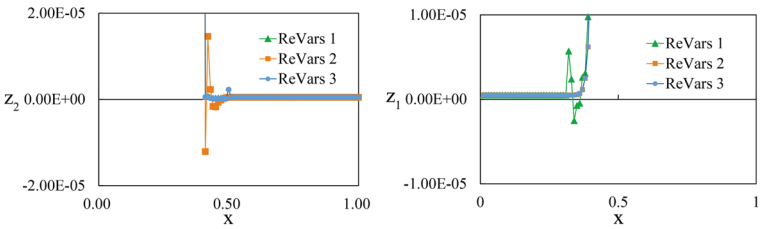

(a) Volume fraction z_2 **(b)** Volume fraction z_1

Fig. 7 Numerical results of the interface-shock interaction problem when different reconstruction variables are used. ReVars 1—advection functions (11), ReVars 2—advection functions (12), ReVars 3—advection functions (13)

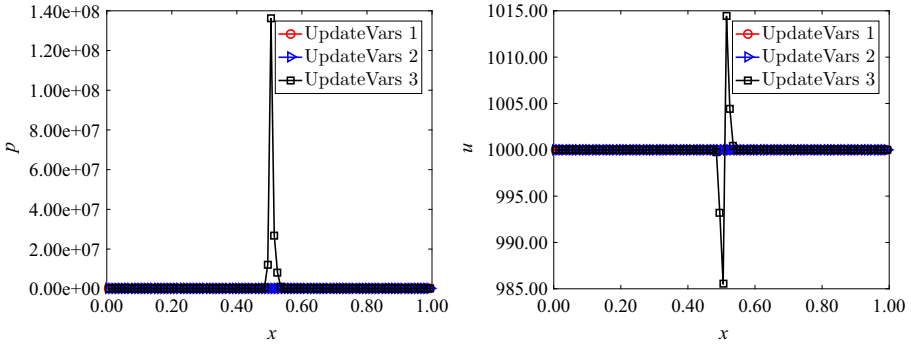

(a) Pressure **(b)** Velocity

Fig. 8 Numerical results of the pure transport problem obtained after 10 time steps on a 100-cell grid with different update variables. UpdateVars 1—advection functions (11), UpdateVars 2—advection functions (12), UpdateVars 3—advection functions (13)

5.5 Pure Transport Problem

We proceed to verify Proposition 7. We reformulate the above problem in Sect. 5.4 as a pure transport problem and assume that uniform velocity 1000.00 and uniform pressure 1.00×10^5 are given as initial data in the computational domain. In the exact solution pressure and velocity should remain constant. We compare the results obtained with the advection functions (11), (12) and (13) as the update variables in Fig. 8. Spurious oscillations are observed in the results obtained with the rational advection functions (13) as update variables. With linear update variables (11) and (12) both pressure and velocity remain constant.

5.6 Interaction of a Shock Wave with a Rectangular Block of SF6

This test is taken from [5]. The computational domain has a rectangular shape (Fig. 9). The Ω_1 domain is filled with the dense gas SF_6 (sulphur hexafluoride), and the Ω_2 domain with air. The gases are in equilibrium at the beginning. A shock wave enters into the computational domain from the left boundary. On the other boundaries reflective boundary conditions are imposed. The shock wave travels through the SF_6 block, and then reflects on the right boundary. The leftward reflected shock wave hits the block again and travels through it. Due to the interaction

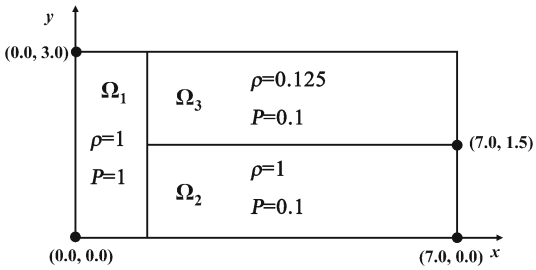

Fig. 9 Configuration for the problem of shock/SF6 block simulations

with the shock wave, the SF_6 block loses its initial rectangular shape and undergoes strong deformation.

The experiment in [5] only involves two domains and two materials. However, since we want to test the ability of our method in dealing with three or more components, this problem is reformulated as a three-material one. Assume that there exists a third domain Ω_3 on the left of the domain Ω_2, as illustrated in Fig. 9. The domain Ω_3 is filled with a material whose thermodynamic parameters are identical with air and the state vector is the same as that assigned at the left boundary LB. This problem statement has no impact on the numerical results, since the left boundary condition remains unchanged. However, the problem in this case can be treated as a three-material problem.

Both air and SF_6 are characterized as perfect gases with adiabatic coefficients $\gamma_{\text{air}} = 1.400$ and $\gamma_{\text{SF6}} = 1.076$, respectively. The initial densities of the SF_6 gas, the air on the left boundary and the air in the domain Ω_2 are 5.805, 1.667 and 1.153, respectively. At the initial moment the gases in domains Ω_1, Ω_2 are at rest with uniform pressure of 96,856.0 Pa. On the left boundary the initial pressure and velocity are 16,3256.0 Pa and (133.273 m/s, 0.0 m/s), respectively.

Figure 10 shows the evolution of the SF_6 block with time. The numerical results obtained on a 450×200 mesh are compared with the experimental results shown in the first column. The results displayed are chosen so as to demonstrate basic stages of this shock interaction process. Figure 10a displays the first interaction of the air shock with the left-hand side of the SF_6 block. Figure 10b displays the situation when the air shock passes by the right-hand side of the SF_6 block. Figure 10c shows the situation when the shock wave in SF_6 reaches the bottom-right corner of the block. In Fig. 10d, the shock wave has reflected from the right end of the tube and is reentering into the block. In Fig. 10e, the reflected shock wave leaves the left-hand side of the block. Figure 10f shows the final stage with highly developed large vortical structures. For detailed analysis of the process see [5].

To check the quantitative correctness of our results, the evolutions of the x-extent and y-extent of the block computed with our algorithm are compared with the experimental and numerical results of [5]. The block interior is taken as a region of the domain with SF6 mass fraction greater than 10%. We can see from Sect. 5.6 that the results of our algorithm are better than those in [5] in the evolution of the left-hand edge of the block, but worse in the evolution of the right-hand edge of the block. The evolution of the upper edge of the block is predicted with good accuracy (Fig. 11).

To check the sharpening effect, we compare the numerical results obtained with and that without the THINC method in Fig. 12. We observe that the THINC method preserves the steepness of the material interfaces very well without spurious oscillations.

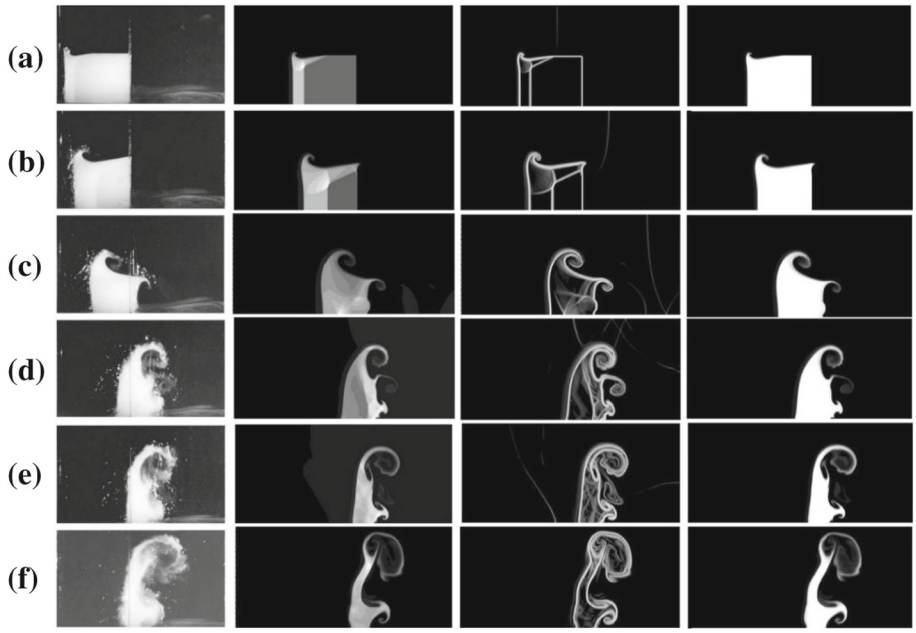

Fig. 10 Comparison between experimental images from [5] (left column: laser-sheet frames) and numerically generated images (second column: density distribution, third column: numerical Schlieren image, right column: distribution of the color function z_2) obtained with the sharpening technique THINC. Times displayed are **a** 206, **b** 446, **c** 926, **d** 1726, **e** 2046, **f** 2846 μs

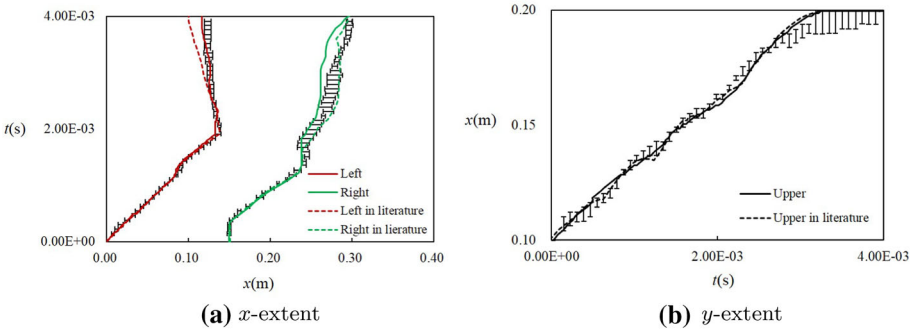

(a) x-extent **(b)** y-extent

Fig. 11 SF_6 block x/y—extent evolution. The solid line shows present numerical results, the dashed line shows the numerical results of [5], error bars show extent measured from experimental frames

5.7 Triple Point Problem

In this section we consider the three-material problem known as triple point problem [17,18,59]. The computational domain is displayed in Fig. 13. This problem is solved as a two-material problem in [18,59]. In the present paper, we assume that the three sub-domains $\Omega_1, \Omega_2, \Omega_3$ are occupied by three different materials which are characterized by the generalized Van der Waals EOS with the parameters listed in Table 2.

Initially all the materials are at rest. The initial density and pressure are displayed in Fig. 13. Reflective boundary conditions are imposed for all the boundaries. A 700 × 300

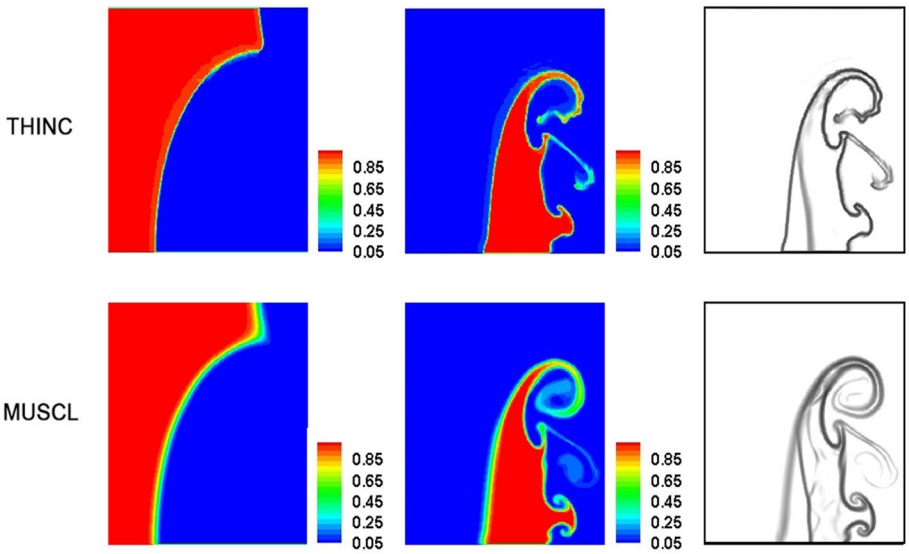

Fig. 12 Comparison of numerical results in domain $[0.16, 0.34] \times [0.00, 0.20]$ obtained with (top) and without (bottom) the sharpening technique THINC. Left column—distribution of the color function z_1, middle column—distribution of the color function z_2, right column—numerical Schlieren (Color figure online)

Fig. 13 Sketch of the triple-point problem

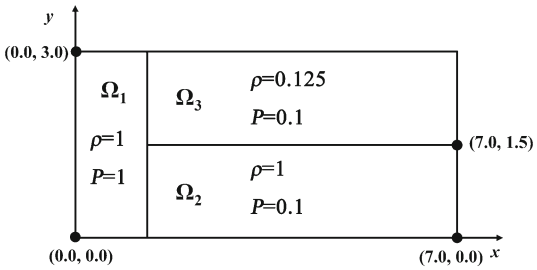

Table 2 Parameters of the gases in the triple point problem

Domain	γ	a (Pa m^6/kg)	b (m^3/kg)	π (Pa)
Ω_1	1.600	1	10^{-3}	0
Ω_2	1.400	0	0	0
Ω_3	1.500	0	0	0

mesh is used for this computation. At a point on the interface between the sub-domain Ω_1 and Ω_3 located sufficiently far from the triple point, three waves are formed because of the breakup of the initial discontinuity, namely, a contact wave, a leftward rarefaction wave and a rightward shock wave. A similar situation occurs at a point on the interface between the sub-domain Ω_1 and Ω_2. The interface between sub domains Ω_2 and Ω_3 represents a contact wave. The shock wave in sub-domain Ω_3 travels faster than the shock wave in sub-domain Ω_2 because of the difference of acoustic impedance in two fluids. Due to velocity difference, the Kelvin–Helmholtz instability is developing along the interface between Ω_2 and Ω_3.

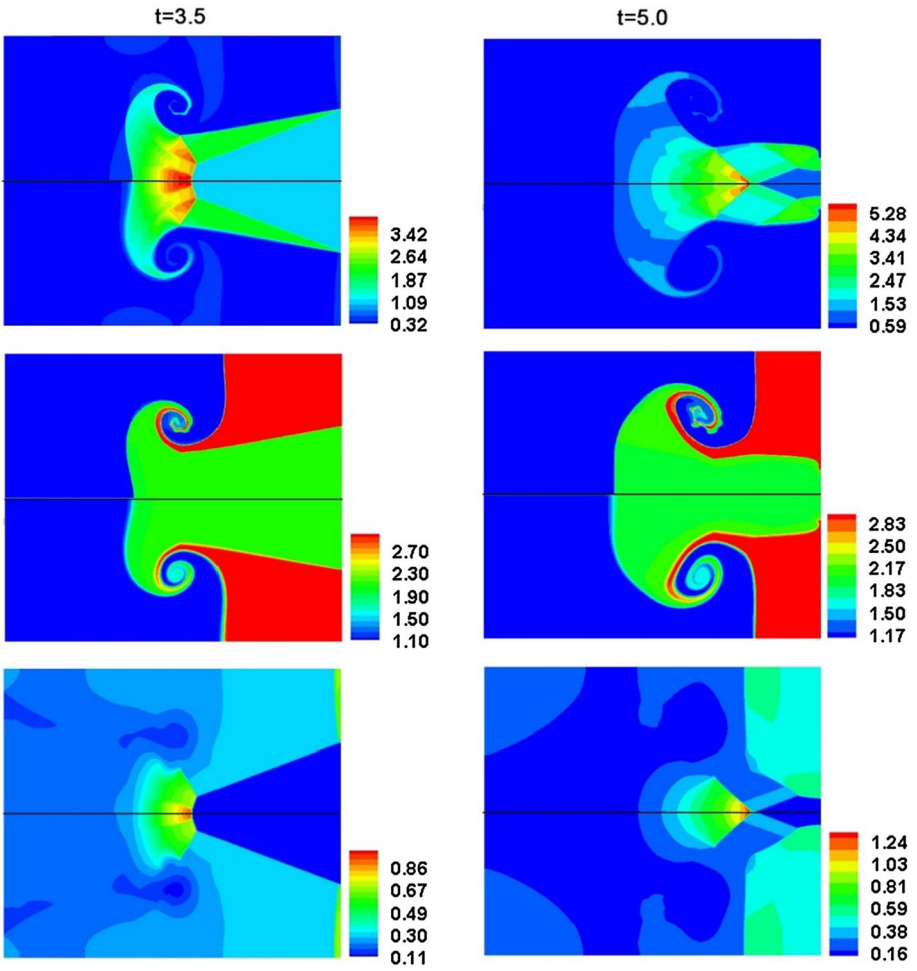

Fig. 14 Numerical results with (top half) and without (bottom half) the sharpening technique THINC of the triple point problem at time $t = 3.5$ (left column) and time $t = 5.0$ (right column). First row—density distribution, second row—distribution of the variable $Z = \sum_{k=1}^{3} kz_k$, third row—pressure distribution

The numerical results are displayed in Fig. 14. The results show a good agreement with the results of [17,18,59]. The Kelvin–Helmholtz instability development is clearly seen. Moreover, our algorithm can also give the distribution of each fluid in the computational domain. Again, the numerical results obtained with our algorithm coupled with the THINC scheme demonstrate more sharpness of the advection front of volume fraction than the second-order MUSCL scheme. No violation of the non-negativity conditions happens throughout the computation.

5.8 Shallow Water Explosion Near a Free Surface

Here we consider an important application of the proposed model—underwater explosion (UNDEX). The underwater explosion near a free surface involves three components: the

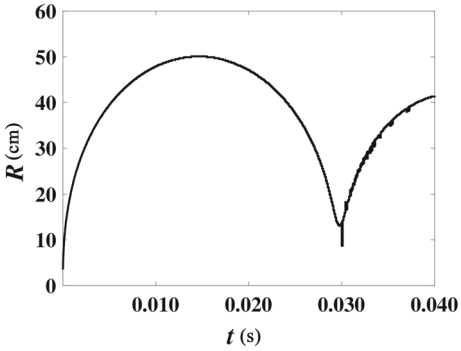

Fig. 15 The evolution of the bubble radius with time

atmosphere air, the water and the explosive gas. Unlike the deep water explosion, in the shallow water explosion the explosive gas may break through the water surface and come into contact with the atmosphere air. However, to the authors' knowledge, almost in all the published works on shallow water explosion, the air and the explosive gas are regarded as the same material, and thus this problem is considered as a simplified two-fluid problem. In our opinion, the main reason for this simplification lies in the difficulty to ensure non-negativity of volume fractions. When EOSs of each material are different, the pressure is very sensitive to volume fractions and any slight violation of the non-negativity conditions leads to the failure of the computation. With the proposed method for ensuring the non-negativity conditions for volume fraction in Sect. 2, we will solve the problem as a three-fluid one.

We first verify our model and numerical methods against the most studied and well-documented two-fluid deep water explosion problem. Consider a spherically symmetric problem—explosion of 300 g TNT at the depth of 94.1 m under the free surface. Both water and explosive gas are characterized with the Mie–Gruneisen EOS—JWL (Jones–Wilkins–Lee) equation:

$$P_k = P_{\infty,k}(\rho_k) + \rho_k \Gamma_k(\rho_k)\left[\varepsilon_k - \varepsilon_{\infty,k}(\rho_k)\right] \tag{61a}$$

$$P_{\infty,k}(\rho_k) = A_{1,k}\exp\left(-\frac{\rho_{0,k}R_{1,k}}{\rho_k}\right) + A_{2,k}\exp\left(-\frac{\rho_{0,k}R_{2,k}}{\rho_k}\right), \tag{61b}$$

$$\varepsilon_{\infty,k}(\rho_k) = \frac{A_{1,k}}{\rho_{0,k}R_{1,k}}\exp\left(-\frac{\rho_{0,k}R_{1,k}}{\rho_k}\right) + \frac{A_{2,k}}{\rho_{0,k}R_{2,k}}\exp\left(-\frac{\rho_{0,k}R_{2,k}}{\rho_k}\right), \tag{61c}$$

where $\rho_{0,k}$, $A_{1,k}$, $A_{2,k}$, $R_{1,k}$, $R_{2,k}$, and Γ_k—the parameters for the k-th component. For water, these parameters are 1.00381 kg/m^3, 1.582×10^{12} Pa, -4.668×10^9 Pa, 8.94, 1.45, and 1.172, respectively. For TNT, they are 1.63 kg/m^3, 3.712×10^{11} Pa, 3.23×10^9 Pa, 4.15, 0.95, and 0.300, respectively [56].

The initial conditions are given as follows: the radius of the explosive gas bubble is 3.5287×10^{-2} m, the pressure and density of the explosive gas are 8.38×10^9 Pa and 1630.00 kg/m^3, respectively; the pressure and density of the surrounding water are 1.0×10^6 Pa and 1025 kg/m^3, respectively. The computational domain is [0 m, 50 m] and discretized with a grid of 25,000 cells. Symmetry and non-reflecting boundary conditions are imposed on the left and right, respectively. Under the above conditions, we have obtained the pulsation process as displayed in Fig. 15. The experimental measurement for the maximum radius of the gas bubble and the pulsation period are 48.10 cm and 29.80 ms, respectively [56]. According to our numerical results these parameters are 50.01 cm and 29.90 ms, respectively and the relative errors are 3.97% and 0.33%, respectively.

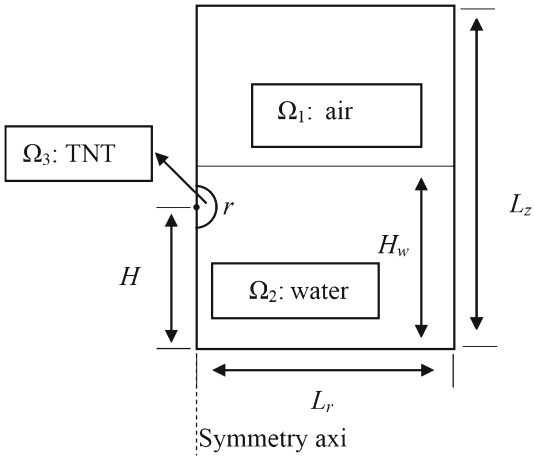

Fig. 16 The configuration of the axisymmetric three-fluid shallow water explosion problem

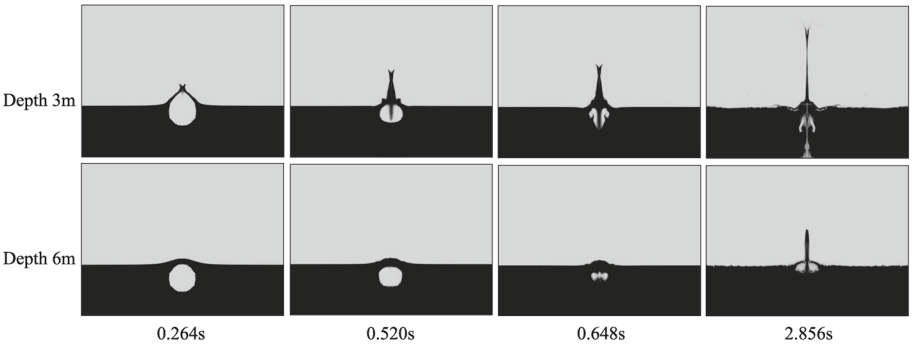

Fig. 17 The evolution of water volume fraction in shallow water explosion problem: first row—explosion at the depth of 3 m, second row—depth 6 m

Further, we proceed with the axisymmetric three-fluid shallow water explosion problem. The geometry configuration is demonstrated in Fig. 16. Unlike the works [35,52,55] where only half pulsation period (that before the maximum bubble radius is reached) is considered, we are interested in the long-term evolution of the explosion process including the burstout of explosive gas into the atmosphere and formation of the so-called "sultan" effect [31] on the free surface.

The geometry parameters are $L_r = 40.00\,\text{m}$, $L_z = 60.00\,\text{m}$, $H_w = 20.00\,\text{m}$, $r = 0.60\,\text{m}$. As in [37], the initial data is given as follows: in atmosphere air, $p = 1.01325 \times 10^5$ Pa, $\rho = 1.225\,\text{kg/m}^3$; in water, the pressure p is given according to statics and $\rho = 1000.000\,\text{kg/m}^3$; inside the explosive gas bubble, $p = 7.2700 \times 10^8$ Pa, $\rho = 240.472\,\text{kg/m}^3$. We consider two cases $H = 17.0\,\text{m}$ (water depth 3 m) and $H = 14.0\,\text{m}$ (water depth 6 m). Computation is performed on a grid of 400×700 cells.

The numerical results for the two cases are displayed in Fig. 17. For both cases the effect of central "sultan" is observed. This effect is also observed experimentally and is described in [31]. The water surface takes a sultan-like shape due to formation of strong cumulative jets at the stage of collapsing of the bubble containing explosion products. In the case of 3 m depth, due to a strong backward cumulative jet, the gas bubble is split up and pushed downwards. Due to the cumulative jets, a central "sultan" is formed. In the case of 6 m depth,

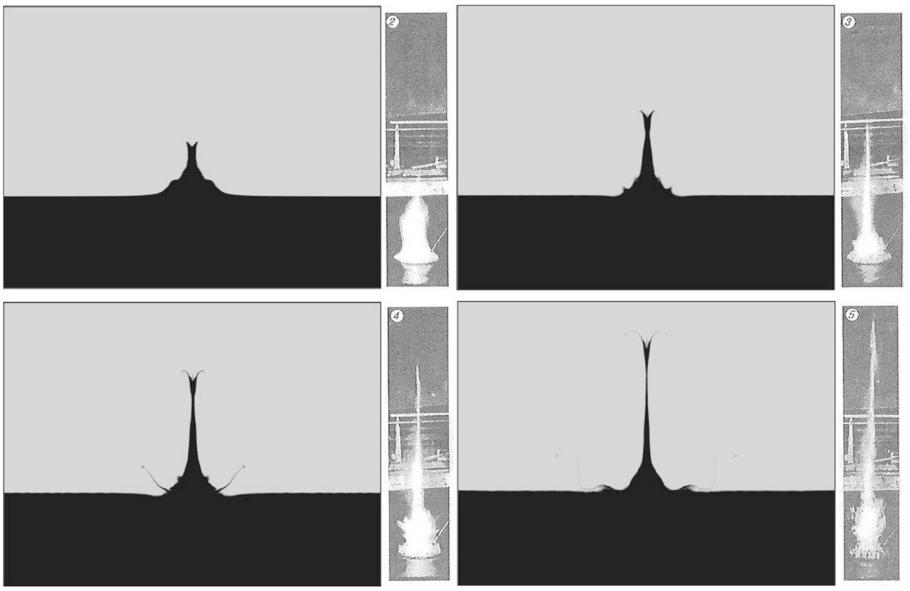

Fig. 18 A qualitative comparison between the numerical results (dept 3 m) and the experimental results in [31] (on the right). Time moments displayed are 0.414 s, 0.552 s, 1.578 s, 2.274 s. The gray color—air, the black color—explosive gas and water

the backward cumulative jet is weaker and the cohesion of the gas bubble is kept. In this case, the pulsation of the bubble is more evident. A qualitative comparison between the numerical results and the experimental results in [31] is demonstrated in Fig. 18. It can be seen that the basic physical effects on the free surface are well captured. Additional details of the simulation results are shown in the attached animation (Online Resource).

6 Conclusions

We have proposed a $(2N + 1)$-equation model for the simulation of multi-fluid flow with $N (N \geq 3)$ compressible materials. The model is based on the single velocity diffuse interface method and includes $N - 1$ advection equations for advection functions. We have proposed specific advection functions for the sub-cell slope reconstruction and updating procedures. For the interpolation procedure, to ensure the non-negativity constraint that any arbitrary partial sum of volume fractions is in the interval [0, 1], we have proposed a set of advection functions in the form of rational functions of volume fractions. With these rational advection functions, any monotonicity-preserving non-linear interpolation schemes and interface-sharpening techniques can be applied without violating the non-negativity constraint for volume fractions or introducing spurious oscillations. Not any modification to these non-linear interpolation schemes are required. Moreover, we proved that the advection functions must be linear with respect to the volume fractions to maintain the PV property in the updating procedure. Thus, we have suggested using different advection functions—rational for reconstruction and linear for updating. Numerical tests demonstrate the efficiency and accuracy of our model and algorithm.

Acknowledgements The first author thanks the China Scholarship Council for their financial support. Computational resources were provided by the Keldysh Institute for Applied Mathematics RAS.

References

1. Abgrall, R.: How to prevent pressure oscillations in multicomponent flow calculations: a quasi conservative approach. J. Comput. Phys. **125**(1), 150–160 (1996)
2. Allaire, G., Clerc, S., Kokh, S.: A five-equation model for the simulation of interfaces between compressible fluids. J. Comput. Phys. **181**(2), 577–616 (2002)
3. Baer, M., Nunziato, J.: A two-phase mixture theory for the deflagration-to-detonation transition (DDT) in reactive granular materials. Int. J. Multiph. Flow **12**(6), 861–889 (1986)
4. Ball, G., Howell, B., Leighton, T., Schofield, M.: Shock-induced collapse of a cylindrical air cavity in water: a free-Lagrange simulation. Shock Waves **10**(4), 265–276 (2000)
5. Bates, K.R., Nikiforakis, N., Holder, D.: Richtmyer–Meshkov instability induced by the interaction of a shock wave with a rectangular block of SF6. Phys. Fluids **19**(3), 323 (2007)
6. Breil, J., Harribey, T., Maire, P.H., Shashkov, M.: A multi-material reale method with MOF interface reconstruction. Comput. Fluids **83**, 115–125 (2013)
7. Cloete, S., Olsen, J.E., Skjetne, P.: CFD modeling of plume and free surface behavior resulting from a sub-sea gas release. Appl. Ocean Res. **31**(3), 220–225 (2009)
8. Cocchi, J.P., Saurel, R.: A Riemann problem based method for the resolution of compressible multimaterial flows. J. Comput. Phys. **137**(2), 265–298 (1997)
9. Coralic, V., Colonius, T.: Finite-volume weno scheme for viscous compressible multicomponent flows. J. Comput. Phys. **274**, 95–121 (2014)
10. Darelius, A., Rasmuson, A., van Wachem, B., Björn, I.N., Folestad, S.: CFD simulation of the high shear mixing process using kinetic theory of granular flow and frictional stress models. Chem. Eng. Sci. **63**(8), 2188–2197 (2008)
11. Després, B., Lagoutière, F.: Contact discontinuity capturing schemes for linear advection and compressible gas dynamics. J. Sci. Comput. **16**(4), 479–524 (2001)
12. Dyadechko, V., Shashkov, M.: Moment-of-fluid interface reconstruction. Los Alamos Report LA-UR-05-7571 (2005)
13. Dyadechko, V., Shashkov, M.: Reconstruction of multi-material interfaces from moment data. J. Comput. Phys. **227**(11), 5361–5384 (2008)
14. Fanneløp, T., Hirschberg, S., Küffer, J.: Surface current and recirculating cells generated by bubble curtains and jets. J. Fluid Mech. **229**, 629–657 (1991)
15. Fedkiw, R.P., Aslam, T., Merriman, B., Osher, S.: A non-oscillatory eulerian approach to interfaces in multimaterial flows (the ghost fluid method). J. Comput. Phys. **152**(2), 457–492 (1999)
16. Friedl, M.J., Fanneløp, T.: Bubble plumes and their interaction with the water surface. Appl. Ocean Res. **22**(2), 119–128 (2000)
17. Friess, M.B., Kokh, S.: Simulation of sharp interface multi-material flows involving an arbitrary number of components through an extended five-equation model. J. Comput. Phys. **273**(273), 488–519 (2014)
18. Galera, S., Maire, P.H., Breil, J.: A two-dimensional unstructured cell-centered multi-material ALE scheme using vof interface reconstruction. J. Comput. Phys. **229**(16), 5755–5787 (2010)
19. Glimm, J., Grove, J.W., Li, X.L., Shyue, K.M., Zeng, Y., Zhang, Q.: Three-dimensional front tracking. SIAM J. Sci. Comput. **19**(3), 703–727 (1998)
20. Glimm, J., Li, X., Liu, Y., Xu, Z., Zhao, N.: Conservative front tracking with improved accuracy. SIAM J. Numer. Anal. **41**(5), 1926–1947 (2003)
21. Ha, C.T., Park, W.G., Jung, C.M.: Numerical simulations of compressible flows using multi-fluid models. Int. J. Multiph. Flow **74**, 5–18 (2015)
22. Harten, A.: The artificial compression method for computation of shocks and contact discontinuities. Math. Comput. **32**(142), 363–389 (1978)
23. Harten, A.: The artificial compression method for computation of shocks and contact discontinuities. Commun. Pure Appl. Math. **30**(5), 611–638 (2010)
24. He, Z., Tian, B., Zhang, Y., Gao, F.: Characteristic-based and interface-sharpening algorithm for high-order simulations of immiscible compressible multi-material flows. J. Comput. Phys. **333**, 247–268 (2017)
25. Hirt, C.W., Nichols, B.D.: Volume of fluid (VOF) method for the dynamics of free boundaries. J. Comput. Phys. **39**(1), 201–225 (1981)
26. Hérard, J.M.: A three-phase flow model. Math. Comput. Modell. **45**(5), 732–755 (2007)

27. Jaouen, S., Lagoutière, F.: Numerical transport of an arbitrary number of components. Comput. Methods Appl. Mech. Eng. **196**(33), 3127–3140 (2007)
28. Johnsen, E., Colonius, T.: Implementation of weno schemes in compressible multicomponent flow problems. J. Comput. Phys. **219**(2), 715–732 (2006)
29. Johnsen, E., Ham, F.: Preventing numerical errors generated by interface-capturing schemes in compressible multi-material flows. J. Comput. Phys. **231**(17), 5705–5717 (2012)
30. Kapila, A., Menikoff, R., Bdzil, J., Son, S., Stewart, D.S.: Two-phase modeling of deflagration-to-detonation transition in granular materials: reduced equations. Phys. Fluids **13**(10), 3002–3024 (2001)
31. Kedrinsky, V.K.: Hydrodynamics of Explosion. Experiment and Models. Publishing House of Siberian Branch of the Russian Academy of Sciences, Siberia (2000). **(in Russian)**
32. Kokh, S., Lagoutière, F.: An anti-diffusive numerical scheme for the simulation of interfaces between compressible fluids by means of a five-equation model. J. Comput. Phys. **229**(8), 2773–2809 (2010)
33. Kucharik, M., Breil, J., Galera, S., Maire, P.H., Berndt, M., Shashkov, M.: Hybrid remap for multi-material ALE. Comput. Fluids **46**(1), 293–297 (2011)
34. Liu, T., Khoo, B., Yeo, K.: The simulation of compressible multi-medium flow: II. Applications to 2D underwater shock refraction. Comput. Fluids **30**(3), 315–337 (2001)
35. Luo, H., Baum, J.D., Löhner, R.: On the computation of multi-material flows using ALE formulation. J. Comput. Phys. **194**(1), 304–328 (2004)
36. Menshov, I., Zakharov, P.: On the composite Riemann problem for multi-material fluid flows. Int. J. Numer. Methods Fluids **76**(2), 109–127 (2015)
37. Miller, S., Jasak, H., Boger, D., Paterson, E., Nedungadi, A.: A pressure-based, compressible, two-phase flow finite volume method for underwater explosions. Comput. Fluids **87**, 132–143 (2013). USNCCM Moving Boundaries
38. Mulder, W., Osher, S., Sethian, J.A.: Computing interface motion in compressible gas dynamics. J. Comput. Phys. **100**(2), 209–228 (1992)
39. Nourgaliev, R.R., Liou, M.S., Theofanous, T.G.: Numerical prediction of interfacial instabilities: sharp interface method (SIM). J. Comput. Phys. **227**(8), 3940–3970 (2008)
40. Olsson, E., Kreiss, G.: A conservative level set method for two phase flow. J. Comput. Phys. **210**(1), 225–246 (2005)
41. Olsson, E., Kreiss, G., Zahedi, S.: A conservative level set method for two phase flow. J. Comput. Phys. **225**(1), 785–807 (2007)
42. Osher, S., Fedkiw, R.: Level Sets and Dynamic Implicit Surfaces. Applied Mathematical Sciences, vol. 153. Springer, Berlin (2002)
43. Osher, S., Sethian, J.A.: Fronts propagating with curvature-dependent speed: algorithms based on Hamilton–Jacobi formulations. J. Comput. Phys. **79**(1), 12–49 (1988)
44. Rzehak, R., Kriebitzsch, S.: Multiphase CFD-simulation of bubbly pipe flow: a code comparison. Int. J. Multiph. Flow **68**, 135–152 (2015)
45. Rzehak, R., Ziegenhein, T., Kriebitzsch, S., Krepper, E., Lucas, D.: Unified modeling of bubbly flows in pipes, bubble columns, and airlift columns. Chem. Eng. Sci. **157**, 147–158 (2017)
46. Saurel, R., Abgrall, R.: A multiphase Godunov method for compressible multifluid and multiphase flows. J. Comput. Phys. **150**(2), 425–467 (1999)
47. Saurel, R., Abgrall, R.: A simple method for compressible multifluid flows. SIAM J. Sci. Comput. **21**(3), 1115–1145 (1999)
48. Saurel, R., Petitpas, F., Berry, R.A.: Simple and efficient relaxation methods for interfaces separating compressible fluids, cavitating flows and shocks in multiphase mixtures. J. Comput. Phys. **228**(5), 1678–1712 (2009)
49. Shin, Y.S., Chisum, J.E.: Modeling and simulation of underwater shock problems using a coupled Lagrangian–Eulerian analysis approach. Shock Vib. **4**(1), 1–10 (1997)
50. Shu, C.: Essentially Non-oscillatory and Weighted Essentially Non-oscillatory Schemes for Hyperbolic Conservation Laws. Springer, Berlin (1998)
51. Shukla, R.K.: Nonlinear preconditioning for efficient and accurate interface capturing in simulation of multicomponent compressible flows. J. Comput. Phys. **276**(276), 508–540 (2014)
52. Shukla, R.K., Pantano, C., Freund, J.B.: An interface capturing method for the simulation of multi-phase compressible flows. J. Comput. Phys. **229**(19), 7411–7439 (2010)
53. Shyue, K.M.: An efficient shock-capturing algorithm for compressible multicomponent problems. J. Comput. Phys. **142**(1), 208–242 (1998)
54. Shyue, K.M.: A fluid-mixture type algorithm for compressible multicomponent flow with Van der Waals equation of state. J. Comput. Phys. **156**(1), 43–88 (1999)
55. Shyue, K.M.: A wave-propagation based volume tracking method for compressible multicomponent flow in two space dimensions. J. Comput. Phys. **215**(1), 219–244 (2006)

56. Shyue, K.M., Xiao, F.: An eulerian interface sharpening algorithm for compressible two-phase flow: the algebraic THINC approach. J. Comput. Phys. **268**(2), 326–354 (2014)
57. So, K.K., Hu, X.Y., Adams, N.A.: Anti-diffusion interface sharpening technique for two-phase compressible flow simulations. J. Comput. Phys. **231**(11), 4304–4323 (2012)
58. Terashima, H., Tryggvason, G.: A front-tracking/ghost-fluid method for fluid interfaces in compressible flows. J. Comput. Phys. **228**(11), 4012–4037 (2009)
59. Tian, B., Shen, W., Jiang, S., Wang, S., Yan, L.: A global arbitrary Lagrangian–Eulerian method for stratified Richtmyer–Meshkov instability. Comput. Fluids **46**(1), 113–121 (2011)
60. Tiwari, A., Freund, J.B., Pantano, C.: A diffuse interface model with immiscibility preservation. J. Comput. Phys. **252**(C), 290–309 (2013)
61. Toro, E.F.: Riemann Solvers and Numerical Methods for Fluid Dynamics. Springer, Berlin (2009)
62. Xiao, F., Honma, Y., Kono, T.: A simple algebraic interface capturing scheme using hyperbolic tangent function. Int. J. Numer. Methods Fluids **48**(9), 1023–1040 (2005)
63. Zhang, C., Menshov, I.: Eulerian modelling of compressible three-fluid flows with surface tension. Russ. J. Numer. Anal. Math. Modell. **34**, 225–240 (2019)
64. Zhang, C., Menshov, I.: Using the composite Riemann problem solution for capturing interfaces in compressible two-phase flows. Appl. Math. Comput. **363**, 124610 (2019)

Affiliations

Chao Zhang[1] · Igor Menshov[2,3]

Igor Menshov
menshov@kiam.ru

1 Department of Computational Mechanics, Lomonosov Moscow State University, Moscow, Russia 119991

2 Keldysh Institute for Applied Mathematics RAS, Moscow, Russia 125581

3 SRISA RAS, Moscow, Russia 117218